Master's Thesis

Evaluation of Circular Polarization Selective Surfaces for Space Applications

LUND UNIVERSITY

Author:
Viktor Liljegren

Supervisor:
Prof. Daniel Sjöberg

April 2013

Abstract

For space applications a circular polarization equivalent of a Dual Gridded Reflector (DGR) would be desirable. Such a structure could be created using Circular Polarization Selective Surfaces (CPSS). In this thesis, various CPSS designs are examined and evaluated for this purpose. The surfaces are evaluated based on how wide a bandwidth can be achieved while staying within requirements on Insertion Loss (IL), Return Loss (RL) and Axial Ratio (AR) as previously used by the European Space Agency (ESA).

The report covers background information on circular polarization, scattering parameters and general CPSS notation that is needed to understand the work as well as more information on the structure requirements. Previously proposed CPSS concepts by Pierrot, Tilston and Morin are explained and a few different implementations based on these concepts are simulated.

The surfaces are designed at 10 GHz and simulated for $8 - 12$ GHz. Each of the structures are simulated for normal incidence as well as for oblique incidence at up to 30°. For the oblique incidence various incidence planes are also examined. The result for each of the simulated structures is presented.

The results are summarized and based on the results it is concluded that the CPSS structures have quite a small bandwidth limited mainly by the AR and that for oblique angles greater than $10° - 20°$ the performance of most of the structures is greatly reduced.

Contents

1 Introduction

When sending information using electromagnetic waves the available frequency bands are limited and it is often desirable to maximize the amount of information sent. One way to do this is to utilize the polarization of the waves to send two channels at the same frequency. By using two orthogonal polarizations it is possible to efficiently separate between the two channels using differently polarized receiver antennas.

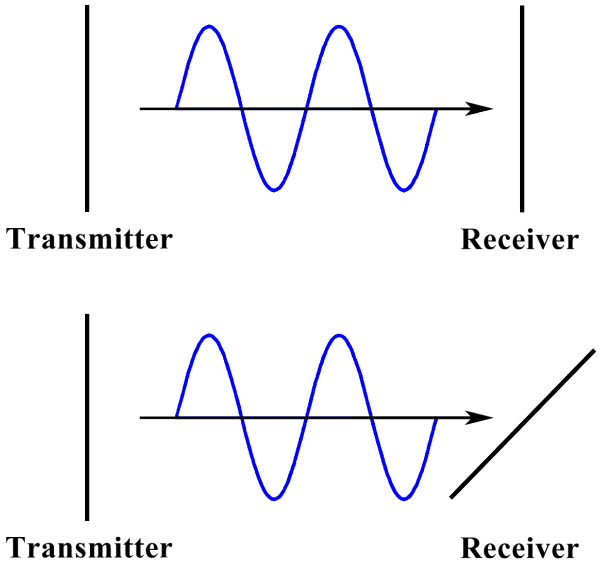

Figure 1: Two sets of transmitter and receiver antennas. At the top the receiver is oriented to receive vertical polarization while at the bottom it is oriented for horizontal polarization. As the transmitted signal is vertically polarized only the top one will receive the signal.

Depending on the implementation either linear or circular polarization can be used. Linear polarization is simple and well understood and changing between polarizations is achieved by rotating the antenna 90°. This however means that to receive a certain polarization the transmitting and receiving antenna must be aligned as demonstrated in Figure 1 [5, pp. 119-120]. If one can see the transmitter as in Figure 1 then achieving this alignment is not a big problem, however when trying to communicate with satellites in space that cannot be seen, it is difficult to set up and maintain proper alignment. Instead circular polarization is preferred, as there is no need to align the transmitter and the receiver [5, pp. 122-123]. The receiving antenna must instead be specifically designed to receive (or transmit) Left Hand Circular Polarization (LHCP) or Right Hand Circular Polarization (RHCP) and the antennas must simply be pointed at each other.

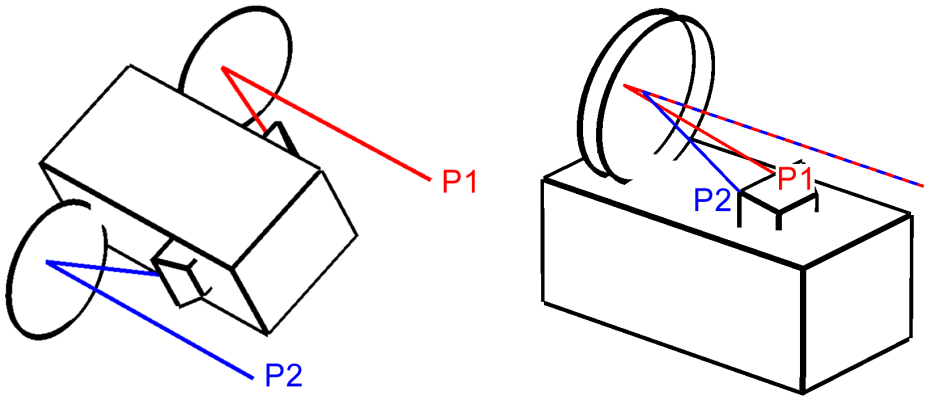

Figure 2: An antenna arrangement using two solid reflectors (left) and an arrangement using a single CPSS reflector to separate the polarizations (right). Figure based on concepts from [14].

A simple configuration to receive two different polarizations on a satellite can be seen on the left in Figure 2. In this arrangement a plane wave containing both polarizations is focused using two solid parabolic dish reflectors onto two different receiving antennas, one which will pick up the LHCP signal and one the RHCP signal. This is however a large and heavy arrangement using two reflectors, so instead a system as can be seen on the right would be preferred.

In this arrangement a two layered reflector would be used [14]. The first layer would reflect one polarization onto the suitable antenna, while at the same time be invisible to the other polarization. The other layer would then focus the remaining polarization onto the other antenna. For linear polarization this could be achieved using a Dual-Gridded Reflector (DGR). A DGR however does not work for circular polarization and so creating a DGR equivalent would be desirable [6].

One way to do this would be to make the reflector out of a Circular Polarization Selective Surface (CPSS) which ideally would function exactly as desired: one polarization would be completely reflected by the surface and one would be completely transmitted. Such surfaces can be constructed [13], however whether their performance is good enough to construct a proper reflector out of them is unclear.

Using performance requirements used by the European Space Agency (ESA) [14] this thesis will attempt to evaluate different CPSS designs to see how well they might function for space applications. How practical the design is from a realization point of view will also to some extent be part of the evaluation.

2 Background

In this section some of the background theory needed to understand the thesis work is detailed. First there is a section on circular polarization which summarizes the basics on how it is defined. This part will also review how oblique incidence is handled.

In the next section the S-parameters used to evaluate the different surfaces are explained. Then a more in-depth definition of CPSS is given together with basic definitions and conventions. In the final section there is a run-down of the structure requirements used to evaluate the CPSS designs, giving the basic CPSS requirements as well as a description of how such a surface could be used and what other alternative approaches could be viable.

Much of the theory in this section is based on the presentation given in [12].

2.1 Circular Polarization

If a time-harmonic wave moves forward in the positive z-direction it can be defined as:

$$\begin{aligned} \boldsymbol{E}_+(z,t) &= \boldsymbol{E}_0 \mathrm{e}^{\mathrm{j}(\omega t - kz)} \\ \boldsymbol{E}_0 &= A_+ \hat{\boldsymbol{x}} + B_+ \hat{\boldsymbol{y}} \end{aligned} \tag{2.1}$$

where A_+ and B_+ are complex constants. The field is complex valued and so the physical wave is represented by $\boldsymbol{E} = \mathrm{Re}(\boldsymbol{E}_+)$. The direction the E-field points in determines the polarization. If either A_+ or B_+ is 0 then the field will only be oscillating in either the $\hat{\boldsymbol{x}}$- or the $\hat{\boldsymbol{y}}$-direction giving a linear polarization. However in the case where $A_+ \neq 0$ and $B_+ \neq 0$ the field could, for a fixed value of z, be tracing a fixed line, a circle or an ellipse.

Expanding the A_+ and B_+ constants into their polar form they become $A_+ = A\mathrm{e}^{\mathrm{j}\phi_a}$ and $B_+ = B\mathrm{e}^{\mathrm{j}\phi_b}$ where A and B are positive magnitudes and ϕ_a and ϕ_b are phases. This gives the complete field:

$$\boldsymbol{E}_+(z,t) = (\hat{\boldsymbol{x}} A\mathrm{e}^{\mathrm{j}\phi_a} + \hat{\boldsymbol{y}} B\mathrm{e}^{\mathrm{j}\phi_b})\mathrm{e}^{\mathrm{j}(\omega t - kz)} = \hat{\boldsymbol{x}} A\mathrm{e}^{\mathrm{j}(\omega t - kz + \phi_a)} + \hat{\boldsymbol{y}} B\mathrm{e}^{\mathrm{j}(\omega t - kz + \phi_b)} \tag{2.2}$$

By using Euler's Formula ($\mathrm{e}^{\mathrm{j}x} = \cos(x) + \mathrm{j}\sin(x)$), $\boldsymbol{E} = \mathrm{Re}(\boldsymbol{E}_+)$ then becomes:

$$\boldsymbol{E}(z,t) = A\cos(\omega t - kz + \phi_a)\hat{\boldsymbol{x}} + B\cos(\omega t - kz + \phi_b)\hat{\boldsymbol{y}} \tag{2.3}$$

If z is then fixed at a specific value, for example $z = 0$ it becomes:

$$\boldsymbol{E}(t) = A\cos(\omega t + \phi_a)\hat{\boldsymbol{x}} + B\cos(\omega t + \phi_b)\hat{\boldsymbol{y}} \tag{2.4}$$

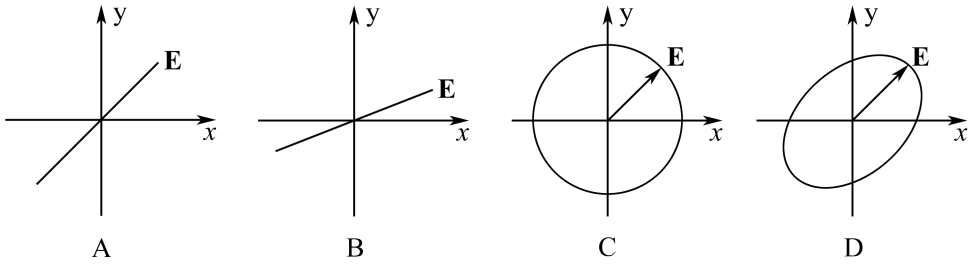

Figure 3: A) Linear polarization, $A = B, \phi_a = \phi_b$ **B)** Linear polarization, $A \neq B, \phi_a = \phi_b$ **C)** Circular polarization, $A = B, \phi_a = \phi_b \pm \frac{\pi}{2}$ **D)** Elliptical polarization

The relation between A, B, ϕ_a and ϕ_b determines the polarization state. The different states can be seen in Figure 3. As long as $\phi_a = \phi_b$ the polarization is linear. If $A = B$ and $\phi_a = \phi_b \pm \frac{\pi}{2}$ the polarization is circular and if none of these cases apply some form of elliptical polarization is achieved.

Assuming the polarization is circular, the exact relation between ϕ_a and ϕ_b will determine the direction of the rotation. If for example $A = B$, $\phi_a = 0$ and $\phi_b = \frac{\pi}{2}$ then the $\boldsymbol{E}$-field becomes:

$$\boldsymbol{E}(t) = A\cos(\omega t)\hat{\boldsymbol{x}} + A\cos(\omega t + \frac{\pi}{2})\hat{\boldsymbol{y}} = A\cos(\omega t)\hat{\boldsymbol{x}} - A\sin(\omega t)\hat{\boldsymbol{y}} \tag{2.5}$$

which represents clockwise rotation around the unit circle in the xy-plane. Similarly for $A = B$, $\phi_a = 0$ and $\phi_b = -\frac{\pi}{2}$ the $\boldsymbol{E}$-field becomes:

$$\boldsymbol{E}(t) = A\cos(\omega t)\hat{\boldsymbol{x}} + A\cos(\omega t - \frac{\pi}{2})\hat{\boldsymbol{y}} = A\cos(\omega t)\hat{\boldsymbol{x}} + A\sin(\omega t)\hat{\boldsymbol{y}} \tag{2.6}$$

which represents counter-clockwise rotation. These two types of rotation are called right and left hand circular polarization (RHCP and LHCP). It is not trivial to determine which is which though. In this thesis the *IEEE convention* is used. According to this convention, if the wave is viewed in the direction of propagation (that is, the wave propagates away from the viewpoint) then a clockwise rotation corresponds to RHCP and counter-clockwise rotation corresponds to LHCP [2].

So far the $\boldsymbol{E}$-field has been represented using x and y components. When dealing with circular polarization it makes sense to introduce new unit vectors, specifically dealing with RHCP and LHCP.

Going back to the complex form, the $\boldsymbol{E}$-field for a circularly polarized wave becomes:

$$\begin{aligned}\boldsymbol{E}_+(z,t) &= A\mathrm{e}^{\mathrm{j}(\omega t-kz+\phi_a)}\hat{\boldsymbol{x}} + A\mathrm{e}^{\mathrm{j}(\omega t-kz+\phi_a\pm\frac{\pi}{2})}\hat{\boldsymbol{y}} \\ &= A(\hat{\boldsymbol{x}} + \hat{\boldsymbol{y}}\mathrm{e}^{\pm\mathrm{j}\frac{\pi}{2}})\mathrm{e}^{j(\omega t-kz+\phi_a)} = A(\hat{\boldsymbol{x}} \pm \mathrm{j}\hat{\boldsymbol{y}})\mathrm{e}^{\mathrm{j}(\omega t-kz+\phi_a)} \quad (2.7)\end{aligned}$$

The new unit vectors can then be easily found as:

$$\hat{\boldsymbol{e}}_+ = \frac{\hat{\boldsymbol{x}} - \mathrm{j}\hat{\boldsymbol{y}}}{\sqrt{2}} \qquad \hat{\boldsymbol{e}}_- = \frac{\hat{\boldsymbol{x}} + \mathrm{j}\hat{\boldsymbol{y}}}{\sqrt{2}} \quad (2.8)$$

Which then relates back to xy-coordinates as:

$$\hat{\boldsymbol{x}} = \frac{\hat{\boldsymbol{e}}_+ + \hat{\boldsymbol{e}}_-}{\sqrt{2}} \qquad \hat{\boldsymbol{y}} = \mathrm{j}\frac{\hat{\boldsymbol{e}}_+ - \hat{\boldsymbol{e}}_-}{\sqrt{2}} \quad (2.9)$$

For a wave that moves in positive z-direction, the $\hat{\boldsymbol{e}}_+$ vector corresponds to RHCP while the $\hat{\boldsymbol{e}}_-$ vector corresponds to LHCP, and vice versa for a wave moving in the negative z-direction.

2.2 Oblique incidence

Not all waves will necessarily hit at normal incidence, it is also possible to have oblique incidence. In order to determine how an oblique wave hits a surface two angles, θ and φ, are defined as in Figure 4.

θ determines the angle of incidence of the incoming wave, while φ determines which incidence plane the wave is travelling in. It is possible for two waves to have the same angle of incidence but be in different incidence planes, as shown in Figure 5 where incidence in the xz-plane ($\varphi = 0°$) and the yz-plane ($\varphi = 90°$) are shown.

It is also possible to define a relation between circular and linear polarization as demonstrated in Section 2.1 for oblique incidence. If a wave, instead of propagating along the z-axis, propagates at an angle θ to the z-axis it will trace an ellipse instead of a circle. If, for example, the wave propagates in the xz-plane ($\varphi = 0°$) the relation becomes:

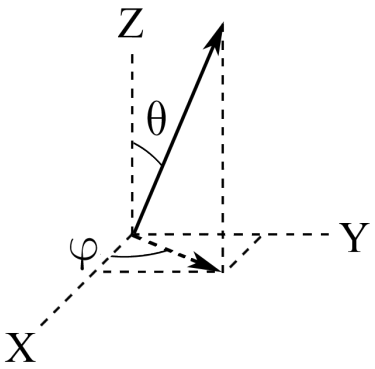

Figure 4: Definition of the θ and φ angles.

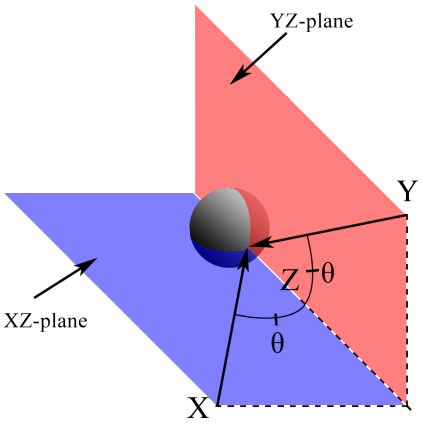

Figure 5: Demonstration of incidence planes. Two waves are hitting the sphere with the same incidence angle θ but in different incidence planes.

$$\hat{\boldsymbol{e}}_+ = \frac{\hat{\boldsymbol{x}}\cos(\theta) - \mathrm{j}\hat{\boldsymbol{y}}}{\sqrt{2}} \qquad \hat{\boldsymbol{e}}_- = \frac{\hat{\boldsymbol{x}}\cos(\theta) + \mathrm{j}\hat{\boldsymbol{y}}}{\sqrt{2}} \tag{2.10}$$

$$\hat{\boldsymbol{x}} = \frac{\hat{\boldsymbol{e}}_+ + \hat{\boldsymbol{e}}_-}{\sqrt{2}\cos(\theta)} \qquad \hat{\boldsymbol{y}} = \mathrm{j}\frac{\hat{\boldsymbol{e}}_+ - \hat{\boldsymbol{e}}_-}{\sqrt{2}} \tag{2.11}$$

Using the same reasoning it is also possible to get the relation for incidence in other planes.

2.3 S-Parameters

When dealing with a large and complex system it can be difficult to characterize it in terms of its individual components, often those components might not even be known or well defined. A more simple way to define the system is to treat it as a black box, that is, to only be concerned about the inputs and the outputs.

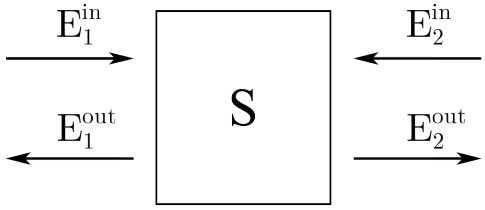

Figure 6: A two-port network with $E_1^{\text{in}}, E_2^{\text{in}}, E_1^{\text{out}}$ and E_2^{out} representing incoming and outgoing waves.

A black box can have any number of input and output ports however a common one is the two-port as can be seen in Figure 6. In this simplified model where the polarization of the fields are not considered the network has two ports, one on the left and one on the right and each port can have a wave going into the black box and one going out of it.

The relation between the waves are defined by the scattering matrix where each element is known as a scattering parameter or S-parameter. The scattering matrix for the two-port in Figure 6 can be seen below:

$$\begin{pmatrix} E_1^{\text{out}} \\ E_2^{\text{out}} \end{pmatrix} = \begin{pmatrix} S_{11} & S_{12} \\ S_{21} & S_{22} \end{pmatrix} \begin{pmatrix} E_1^{\text{in}} \\ E_2^{\text{in}} \end{pmatrix} \tag{2.12}$$

This gives the relationship between the waves as follows:

$$\begin{aligned} E_1^{\text{out}} &= S_{11}E_1^{\text{in}} + S_{12}E_2^{\text{in}} \\ E_2^{\text{out}} &= S_{21}E_1^{\text{in}} + S_{22}E_2^{\text{in}} \end{aligned} \tag{2.13}$$

However, measurement of S-parameters are supposed to be done by sending one wave at a time, and connecting a matched load to the other input. This means that the S-parameters become defined as:

$$
\begin{aligned}
S_{11} &= \left.\frac{E_1^{\text{out}}}{E_1^{\text{in}}}\right|_{E_2^{\text{in}}=0} & S_{12} &= \left.\frac{E_1^{\text{out}}}{E_2^{\text{in}}}\right|_{E_1^{\text{in}}=0} \\
S_{21} &= \left.\frac{E_2^{\text{out}}}{E_1^{\text{in}}}\right|_{E_2^{\text{in}}=0} & S_{22} &= \left.\frac{E_2^{\text{out}}}{E_2^{\text{in}}}\right|_{E_1^{\text{in}}=0}
\end{aligned}
\tag{2.14}
$$

S_{11} and S_{22} are generally known as reflection coefficients as they describe the relation between the reflected and incident wave. S_{12} and S_{21} are similarly known as transmission coefficients since they describe the relation between the transmitted and incident wave.

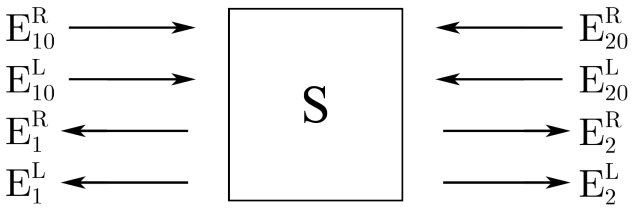

Figure 7: A four-port network treating LHCP and RHCP polarizations as different waves.

For measurements in this thesis, S-parameters will be used to measure the difference between the incoming and outgoing $\boldsymbol{E}$-field. However, since it is important to differentiate between the polarizations, each field now has to be treated as two different inputs making the whole system a 4-port as seen in Figure 7 where the total $\boldsymbol{E}$-fields are divided into LHCP and RHCP fields:

$$\boldsymbol{E}_1^{\text{out}} = E_1^{\text{R}}\hat{\boldsymbol{e}}_- + E_1^{\text{L}}\hat{\boldsymbol{e}}_+ \tag{2.15}$$

$$\boldsymbol{E}_2^{\text{out}} = E_2^{\text{R}}\hat{\boldsymbol{e}}_+ + E_2^{\text{L}}\hat{\boldsymbol{e}}_- \tag{2.16}$$

$$\boldsymbol{E}_1^{\text{in}} = E_{10}^{\text{R}}\hat{\boldsymbol{e}}_+ + E_{10}^{\text{L}}\hat{\boldsymbol{e}}_- \tag{2.17}$$

$$\boldsymbol{E}_2^{\text{in}} = E_{20}^{\text{R}}\hat{\boldsymbol{e}}_- + E_{20}^{\text{L}}\hat{\boldsymbol{e}}_+ \tag{2.18}$$

This four-port then gives a 4x4 scattering matrix as:

$$
\begin{pmatrix} E_1^{\text{R}} \\ E_1^{\text{L}} \\ E_2^{\text{R}} \\ E_2^{\text{L}} \end{pmatrix} = \begin{pmatrix} S_{11}^{\text{RR}} & S_{11}^{\text{RL}} & S_{12}^{\text{RR}} & S_{12}^{\text{RL}} \\ S_{11}^{\text{LR}} & S_{11}^{\text{LL}} & S_{12}^{\text{LR}} & S_{12}^{\text{LL}} \\ S_{21}^{\text{RR}} & S_{21}^{\text{RL}} & S_{22}^{\text{RR}} & S_{22}^{\text{RL}} \\ S_{21}^{\text{LR}} & S_{21}^{\text{LL}} & S_{22}^{\text{LR}} & S_{22}^{\text{LL}} \end{pmatrix} \begin{pmatrix} E_{10}^{\text{R}} \\ E_{10}^{\text{L}} \\ E_{20}^{\text{R}} \\ E_{20}^{\text{L}} \end{pmatrix}
\tag{2.19}
$$

where the scattering parameters are defined as $S_{mn}^{kl} = E_m^k / E_{n0}^l$, assuming that E_{n0}^l is the only input field. For example $S_{12}^{\mathrm{RL}} = E_1^{\mathrm{R}} / E_{20}^{\mathrm{L}}$. While the matrix is significantly larger than the 2x2 case, the fundamentals are still the same, such that S_{12} and S_{21} parameters are transmission. coefficients and S_{11} and S_{22} parameters are reflection coefficients. For example, S_{11}^{RR} represents a reflection coefficient for an incident wave at port 1 with an RHCP polarization where the reflected wave also has RHCP polarization.

While the S-parameters are a powerful tool when analysing a system, they are often manipulated to more clearly show results that are of interest. The following definitions are used in this thesis.

2.3.1 Return loss (RL)

The return loss is defined as the ratio in decibels of the power of a wave incident to a discontinuity relative to the power of the wave reflected by the discontinuity [1]. Using S-parameters the RL is defined as:

$$\mathrm{RL} = -20 \log_{10} \left(\left| S_{mm}^{kl} \right| \right) \tag{2.20}$$

Often the return loss is only interesting for co-polarized components ($l = k$) as this represents a more pure reflection. As can be seen in the definition, the return loss is always a positive value unless the reflected wave has more power than the incident wave, which is only possible with an active system.

2.3.2 Insertion loss (IL)

The insertion loss is defined as the ratio of the power transmitted between two ports before the insertion of a load between them relative to the power transmitted after the load is inserted [1]. In terms of S-parameters it is defined as:

$$\mathrm{IL} = -20 \log_{10} \left(\left| S_{mn}^{kk} \right| \right), m \neq n \tag{2.21}$$

As with the return loss, the IL is positive unless the system is active and works as an amplifier.

2.3.3 Axial ratio (AR)

The axial ratio refers to the ratio between the major and minor axis of the polarization ellipse [2]. In the case of fully circular polarization the major and minor

axes are the same and the AR is 1 (0 dB), otherwise it represents how elliptical the polarization is. Since mixing RHCP and LHCP results in an overall elliptical polarization the AR is a good way of measuring how pure the polarization is.

Assuming the major(A) and minor(B) axes are known, the AR would be defined as A/B. Considering the complex wave $\boldsymbol{E} = E_{\mathrm{R}}\hat{\boldsymbol{e}}_{+} + E_{\mathrm{L}}\hat{\boldsymbol{e}}_{-}$, the Stokes parameters provide a way to link the magnitudes of the wave to its major and minor axes and eventually calculating the AR. The Stokes parameters are defined as follows [8, p. 301]:

$$I = |E_{\mathrm{L}}|^2 + |E_{\mathrm{R}}|^2\,, \quad Q = 2\mathrm{Re}\left(E_{\mathrm{R}}^{*}E_{\mathrm{L}}\right), \quad U = 2\mathrm{Im}\left(E_{\mathrm{R}}^{*}E_{\mathrm{L}}\right), \quad V = |E_{\mathrm{L}}|^2 - |E_{\mathrm{R}}|^2 \tag{2.22}$$

Combing the Stokes parameters with $I_{\mathrm{p}} = \sqrt{Q^2 + U^2 + V^2}$, the total polarization intensity and $L = Q + \mathrm{j}U$, the complex intensity of linear polarization, the major and minor axes can be found as [12, p. 50]:

$$A = \sqrt{\frac{1}{2}\left(I_{\mathrm{p}} + |L|\right)} \qquad\qquad B = \sqrt{\frac{1}{2}\left(I_{\mathrm{p}} - |L|\right)} \tag{2.23}$$

The axial ratio can then be calculated by:

$$\left(\frac{A}{B}\right)^2 = \frac{\sqrt{Q^2+U^2+V^2} + \sqrt{Q^2+U^2}}{\sqrt{Q^2+U^2+V^2} - \sqrt{Q^2+U^2}} = \frac{\sqrt{1+\alpha}+1}{\sqrt{1+\alpha}-1} \tag{2.24}$$

where α is defined as (assuming E_{n0}^{l} as the input wave):

$$\begin{aligned}\alpha = \frac{V^2}{Q^2+U^2} &= \frac{\left(\left|S_{mn}^{kl}\right|^2 - \left|S_{mn}^{ll}\right|^2\right)^2}{\left[2\mathrm{Re}\left(\left(S_{mn}^{kl}\right)^{*} S_{mn}^{ll}\right)\right]^2 + \left[2\mathrm{Im}\left(\left(S_{mn}^{kl}\right)^{*} S_{mn}^{ll}\right)\right]^2} \\ &= \frac{\left(\left|S_{mn}^{kl}\right|^2 - \left|S_{mn}^{ll}\right|^2\right)^2}{\left[2\left(S_{mn}^{kl}\right)^{*} S_{mn}^{ll}\right]^2} = \frac{1}{4}\left(\left|\frac{S_{mn}^{kl}}{S_{mn}^{ll}}\right| - \left|\frac{S_{mn}^{ll}}{S_{mn}^{kl}}\right|\right)^2\end{aligned} \tag{2.25}$$

where $k \neq l$ must apply. If $m = n$ the AR refers to reflection and if $m \neq n$ it refers to transmission. Note that whether S_{mn}^{kl} corresponds to E_R or E_L depends on whether the incoming wave E_{n0}^{l} is LHCP or RHCP. Due to the symmetry and the square however, the placement of the complex conjugate is not a factor hence this can be safely ignored. The axial ratio in dB can be given as:

$$\mathrm{AR} = 20\log_{10}\left(\frac{A}{B}\right), \quad k \neq l \tag{2.26}$$

An alternative way to measure the polarization purity is by using the Cross-polarization discrimination (XPD) which is defined as the ratio of the average received power of the desired polarization (co-polarized) relative to the average received power of the undesired one (cross-polarization) [10] and can be calculated as:

$$\mathrm{XPD} = 20\log_{10}\left(\left|\frac{S_{mn}^{kk}}{S_{mn}^{kl}}\right|\right), k \neq l \tag{2.27}$$

The XPD is generally equivalent to the AR when measuring polarization purity, however in this thesis only AR will be used.

2.4 CPSS

A circular-polarization-selective surface (CPSS) is defined as a surface which will reflect one circular polarization (left or right) while at the same time be transparent to the other polarization [14]. How to design a CPSS is not trivial, and in fact it has been argued that such a surface cannot be physically realized [4, pp. 322-323] although this was later disproved in [13]. Actual designs on how to construct a CPSS however are described in Section 3 as this section will only deal with the basic definitions of how a CPSS should behave.

The definition of a CPSS does not state which polarization should be reflected and which should be transmitted. To make the distinction more clear a CPSS which reflects LHCP polarized waves will be referred to as a left-hand circular-polarization-selective surface (LHCPSS). Similarly a CPSS which reflects RHCP is called an RHCPSS. Aside from the difference in which polarization the two should function identically, so for simplicity the rest of the definitions will assume an LHCPSS structure is used.

The CPSS definition does not state specifics of what happens to a wave after it has been reflected or transmitted, as such four different types of CPSS can be envisioned [13]. The different types for an LHCPSS can be seen in Figures 8-11.

For type A and B the handedness of the reflected wave remains the same as the incident one while it changes for type C and D. The reciprocity principle of electromagnetism states that for a reciprocal structure, the operation remains unchanged if the direction is reversed but the polarization remains the same. This can be seen to apply for type A and B, but not for C and D. Therefore A and B are referred to as reciprocal while C and D are non-reciprocal.

For the reciprocal structures, type A reflects LHCP both from the right and from the left, and any transmitted wave maintains its handedness. For type B on the

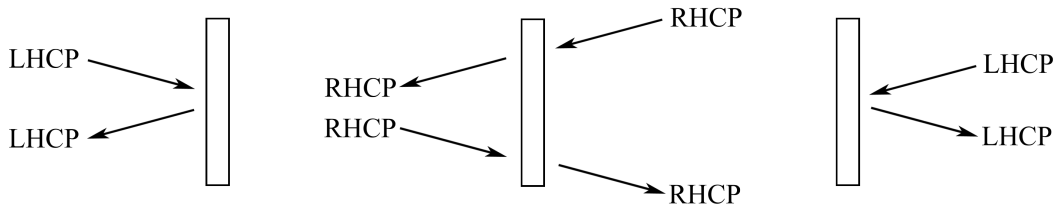

Figure 8: The operation of a reciprocal - symmetrical LHCPSS (Type A).

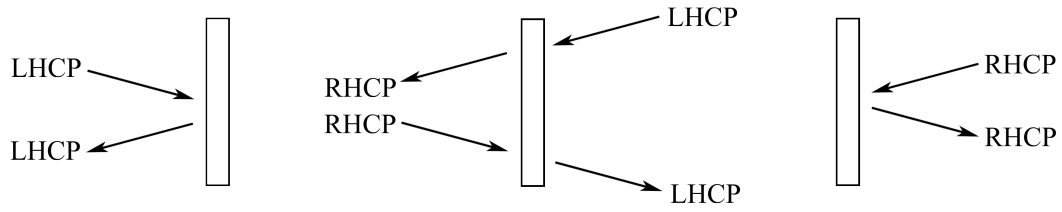

Figure 9: The operation of a reciprocal - asymmetrical LHCPSS (Type B).

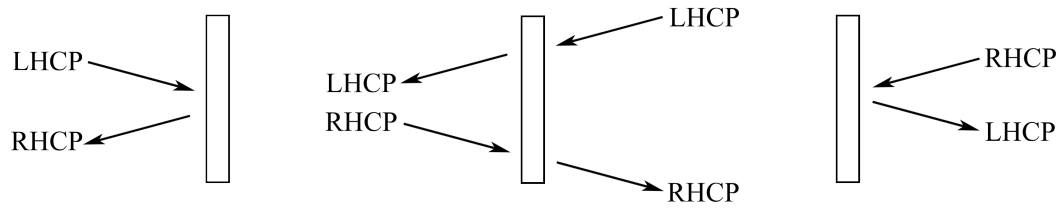

Figure 10: The operation of a non-reciprocal - symmetrical LHCPSS (Type C).

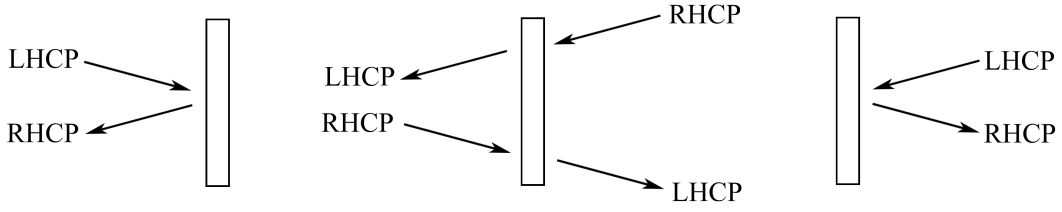

Figure 11: The operation of a non-reciprocal - asymmetrical LHCPSS (Type D).

other hand, the handedness of a transmitted wave changes, and the left and right side reflects different polarizations. Due to this difference, type A is referred to as symmetrical, while type B is asymmetrical.

Using a similar definition for the non-reciprocal structures, for type C a transmitted wave maintains its handedness while it does not for type D. Based on the similarities with the reciprocal case type C is called symmetrical while type D is called asymmetrical.

While there are potential usages of the non-reciprocal surfaces, the fact that they result in non-reciprocal scattering implies that they are not reciprocal devices [13] and cannot be made of only reciprocal materials such as metallic wires. This is problematic when trying to design a simple structure for space applications. For the reciprocal surfaces however, there are currently no previously suggested designs for a reciprocal-asymmetric (type B) surface. As such, only reciprocal-symmetrical CPSS structures are examined and unless otherwise stated, whenever a CPSS is mentioned it will refer to the reciprocal-symmetrical variety.

2.5 Structure requirements

The requirements set for the CPSS surface is based on ideas from the European Space Agency (ESA) on how such a surface could be used [6, 14]. Currently the main problem is that while circular polarization is very practical for space applications, two separate solid reflector antennas have to be used on the satellite to separate between the two channels (as was previously seen in Figure 2).

For linear polarization a structure known as a dual-gridded reflector (DGR) can be used to separate two orthogonal polarizations and focus them at different points, as illustrated in Figure 12. If an equivalent structure could be designed for circular polarization there would be several advantages. For example, by combining the two solid reflectors into a single unified one the size and weight is reduced. Another advantage is that by separating the polarizations before they reach the antenna the polarization purity of the signal is increased which reduces the cross-talk between the two channels.

To create a DGR-like reflector for circular polarization ESA has suggested three different approaches using CPSS surfaces [6]. These can be seen in Figure 13. Two of the suggestions use non-reciprocal CPSS surfaces which as explained in Section 2.4 is not suitable for space applications. As such, the most appropriate CPSS based suggestion is type A in Figure 13.

Since the CPSS will be used to form a parabolic dish, waves will not hit it at

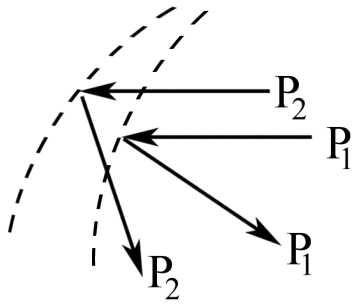

Figure 12: The two polarizations P_1 and P_2 are reflected in different directions by the DGR.

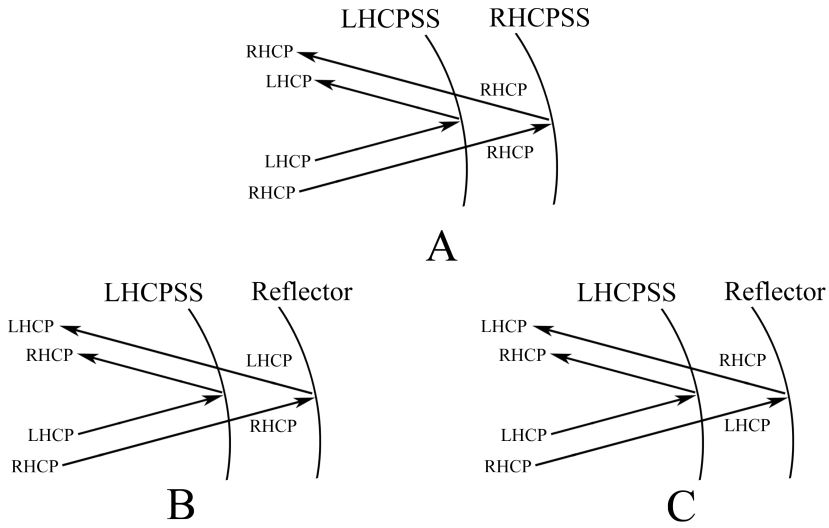

Figure 13: Circular polarization equivalent of a DGR using **A)** two reciprocal - symmetrical CPSS surfaces **B)** one reflector and one non-reciprocal - symmetrical CPSS **C)**one reflector and one non-reciprocal - asymmetrical CPSS.

normal incidence. The dish might be angled such that waves hit the center at, for example, a 20° angle. The surface must therefore be able to function even for oblique angles. Additionally each part of the wave will not hit at the same angle, so the surface must also be able to handle variance around the center angle. There are no set requirements here as they depend on the implementation of the dish in the broader antenna system, however the greater variance that can be achieved the more freedom is allowed when designing the dish. In an application to ESA there are a few different proposals for how the full system could look [7]. In this application, the largest angle of incidence in a proposed concept is 36.9° while most of the concepts were in the $20° - 30°$ span. For the sake of simplicity, each design in this thesis will be tested at up to 30°.

Additionally, the smallest variance in angle of incidence was 13.6°, as such it is considered that the designs must at least be capable of a 10° angle of incidence to be able to have any usage.

Another requirement is that the CPSS should be made of materials practical for usage in space. Ideally the surface would be made only out of metals although some dielectric materials can also be used.

There are also requirements when it comes to the reflective and transmissive properties of the CPSS. While actual performance requirements are set not for the CPSS surface alone but for the entire system [6], ESA themselves have been working on well defined requirements of an IL and RL lower than 0.5 dB. Since the surface is supposed to give greater polarization purity, there is also a requirement of an AR lower than 0.75 dB [14]. These requirements will form the basis of the evaluation of the CPSS surfaces examined in this thesis.

While there are several different frequency bands where the surfaces could operate, in ESA's previous CPSS tests they designed it to function around 10 GHz [14]. There were no bandwidth requirements, rather it was desired to get as great bandwidth as possible. Based on this, in this thesis the designs will be examined between $8 - 12$ GHz with no minimum bandwidth requirements but with a goal to get it as large as possible.

As a final requirement, each of the CPSS structures will consist primarily of thin metal wires and in order to ensure some structural stability the wire diameter, called a, must be at least 0.2 mm. All of the goals and requirements stated above can be summarized as:

- **IL** ≤ 0.5 dB
- **RL** ≤ 0.5 dB
- **AR** ≤ 0.75 dB
- *IL, RL and AR bandwidth should be as wide as possible*
- *The structures should be examined at up to* 30° *angle of incidence*
- *The structures should be able to handle at least* 10° *variance in angle of incidence*
- *The structures will be designed for operation at* 10 GHz($\lambda = 30$ mm) *and simulated for* $8 - 12$ GHz
- *The wire diameter, a, must be at least* 0.2 mm

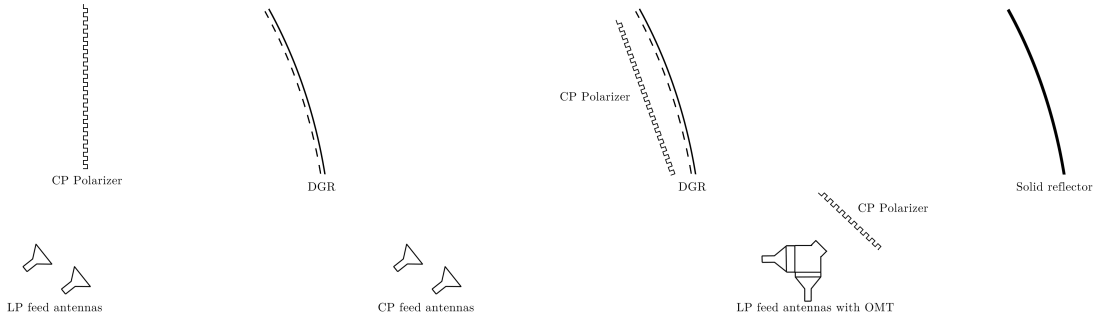

Figure 14: Three concepts using polarizers instead of CPSS surfaces [3].

As an aside, while the CPSS solution is the one that is of interest in this thesis it is not the only possible structure that ESA proposes. Another possible solution is to use polarizers to go from circular to linear polarization and do the polarization selection in linear polarization where such operations are easier [6]. A few proposed concepts can be seen in Figure 14. Such solutions are perhaps not as elegant as a CPSS one and the placement of the polarizer can be problematic. However as polarization selection is more well understood in linear polarization it might lead to a more robust solution.

Another proposed use of polarizers is to use them to create a CPSS by first using a polarizer to switch to linear polarization, then doing the polarization selection and finally have another set of polarizers to switch back to circular polarization. Such a CPSS has previously been made [9], a problem with this design however is that each polarizer actually need to consist of several cascaded polarizer layers in order to achieve proper polarization purity. This means that the full CPSS becomes significantly thicker than using a single inherently selective surface.

2.6 Simulation software

To evaluate the different CPSS designs they will be simulated using the commercial software CST Microwave Studio (*CST Computer Simulation Technology AG*, http://www.cst.com/). The simulation method used by CST is the Finite Integration Technique (FIT) [16], although in the frequency domain the implementation is very similar to the Finite Element Method (FEM) as described in [15]. The method works by solving Maxwell's equation in their integral form unlike many other numerical methods which solve them in their differential form [16]. Explicitly, the equations on integral form are given by:

$$\begin{aligned} \oint_{\partial S} \boldsymbol{E} \cdot \mathrm{d}\boldsymbol{r} &= -\int_{S} \frac{\partial \boldsymbol{B}}{\partial t} \cdot \mathrm{d}\boldsymbol{S} & \oint_{\partial S} \boldsymbol{H} \cdot \mathrm{d}\boldsymbol{r} &= \int_{S} \left(\frac{\partial \boldsymbol{D}}{\partial t} + \boldsymbol{J} \right) \cdot \mathrm{d}\boldsymbol{S} \\ \oint_{\partial V} \boldsymbol{D} \cdot \mathrm{d}\boldsymbol{S} &= \int_{V} \rho \cdot \mathrm{d}\boldsymbol{V} & \oint_{\partial V} \boldsymbol{B} \cdot \mathrm{d}\boldsymbol{S} &= 0 \end{aligned} \tag{2.28}$$

In order to solve these equations numerically, a finite calculation domain must be defined such that it encloses the considered problem. In order to do this CST creates a mesh of the domain and the structure, and then formulates Maxwell's equations for each cell separately. This can then be summarized into a large matrix problem to solve for the entire domain.

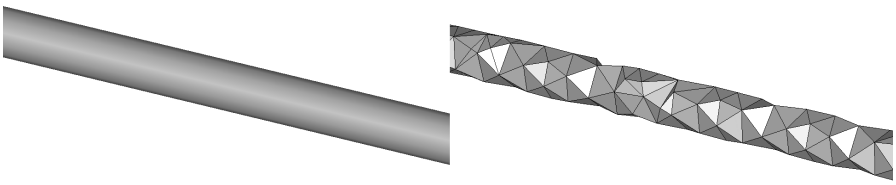

Figure 15: The smooth wire on the left has been meshed by CST for the simulation.

Due to the discrete mesh there are numerical inaccuracies introduced. How large these errors are depends on the complexity of the simulated structure and on how fine the meshing is. How fine the mesh should be then becomes a balancing act between available memory, simulation time and acceptable error size. In order to improve the results and performance CST does have certain tools to improve the meshing, there is for example an adaptive mesh option which will estimate the error during the simulation and then improve the mesh in areas where the error is estimated to be high. CST does provide guidelines for mesh settings which are followed for all of the simulations in the results.

CST Microwave Studio provides two different solvers for calculating the S-parameters, the Transient Solver and the Frequency Domain Solver. The Frequency Domain Solver is recommended for use in, among other, cases with unit cell boundaries. Since each of the CPSS designs examined are unit cells in a larger periodic structure this is the solver used. In a sweep over several frequencies, the solver will solve the problem for one frequency at the time and chooses which frequencies to compute adaptively and interpolates the others.

A useful feature of CST is that it allows for post processing of all calculated data. This means that it is possible to calculate the IL, RL and AR from the S-parameters

as specified in Section 2.3 directly in CST without the need to first export them to an outside program. This post processing is also useful to define goals for the built in optimizer. By defining goals to keep the IL, RL and AR below the defined limits CST can optimize the system more efficiently than manual iteration. CST offers several different optimization algorithms, the one used is the default Trust Region Framework which CST claims is the most modern.

There are several different settings available in CST not mentioned in this section. In general if a setting is not mentioned then it has been left to its default value.

During most of the work, CST's internal post processing was used to examine the S-parameters, however at the end there was a need to export the final S-parameters for external processing. While the theoretical scattering matrix for circular polarization can be seen in Equation (2.19), it is not certain that the scattering matrix exported by CST is organized like this.

In order to verify the element numbering of the S-matrix from CST, a linear polarizer was simulated. Since such a shape has a well known theoretical S-matrix. In [14] a Pierrot cell with well explained dimensions was experimentally tested and IR, RL and AR data was provided. By recreating and simulating this cell in CST combined with the linear polarizer it was possible to figure out the transformation needed to rearrange the exported matrix into the theoretical one. More information on the verification can be found in Appendix A.

3 CPSS designs

In this section various CPSS concepts will be explained. First in sub-section 3.1 three previously proposed designs will be introduced in their purest form and the basic theory of how they work will be explained. In Section 3.2 various implementations of these basic concepts are introduced. The implementation includes basics such as which parameter of the design can be altered, but also some alternative designs based on the basic concepts. The designs introduced in this sub-section are the ones that will be simulated later.

Each of the concepts introduced will consist of small cells each working as a CPSS. The full surface however will consists of several of these cells repeated in order to cover a large area.

3.1 Basic concepts

3.1.1 Pierrot

The oldest known design was first introduced by Pierrot in a French patent in 1966 16 [13]. It is the simplest of the designs and is essentially a bent wire as can be seen in Figure.

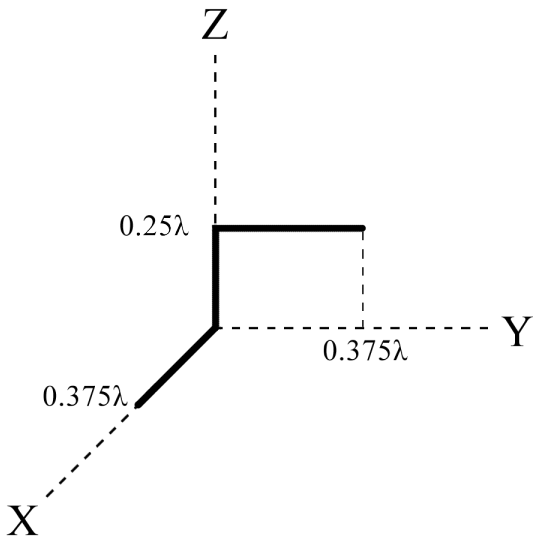

Figure 16: Geometry of a Pierrot cell. The figure depicts an LHCPSS (assuming the wave is travelling in the positive z-direction).

The idea behind the design is based on the fact that a circularly polarized wave can be broken up into two linearly polarized components as explained in section 2.1. A wire stretched out in one direction will only react to waves polarized in that direction. That is, if a wire lies in the x-direction it will only react to the part of the wave that is polarized in the x-direction and not to the part that is polarized in the y-direction. On the other hand, a wire that lies in the direction of propagation(z-direction) will not react to the wave at all.

When moving along a circularly polarized wave, it takes one wavelength for the wave vector to rotate one full revolution. As such, moving a quarter wavelength is the same as rotating a quarter of a revolution. If the circularly polarized wave in the current location is entirely in the positive x-direction, a quarter of a wavelength further ahead it will be entirely in the positive or negative y-direction(depending on whether the wave is LHCP or RHCP).

An LHCP wave illuminating the LHCPSS in Figure 16 at normal incidence will trace a right handed helix along the z-axis and induce currents along the x- and y-aligned parts of the wire. The wave will induce a current in the wire, and due to the quarter wavelength difference between the transverse parts, when it induces a current in the x-direction it will also induce an in-phase current in the y-direction. These induced currents will add in-phase along the entire wire. The overall current distribution becomes sinusoidal with the null at the center of the z-aligned part.

Due to the total wire length of one wavelength the wire will be operating at a resonance and each of the transverse arms can now be seen as dipoles, radiating in the positive and negative z-direction. Due to the quarter wavelength difference between the arms, the radiated wave will gain an LHCP polarization in both directions. In the positive z-direction however, it will be out of phase with the illuminating wave, to ideally completely block all transmission and reflect the entire wave.

If the cell is instead illuminated by an RHCP wave, the wave will trace a left handed helix and the induced currents will now add out of phase along the entire wire. The wire will no longer be at resonance and the overall current will be very weak. The wire will ideally not radiate any wave and the entire illuminating wave will be transmitted.

3.1.2 Tilston

The second design was introduced by Tilston 16 [13]. Like the Pierrot cell it relies on the linear components of the circularly polarized wave and a quarter wavelength

division between the two components. There are however quite a few differences in how they are used.

The Tilston cell consists of two dipoles, connected together by a transmission line as can be seen in Figure 17 [13]. Which ends of the dipoles are connected together by the transmission line determines whether it is an LHCPSS or RHCPSS.

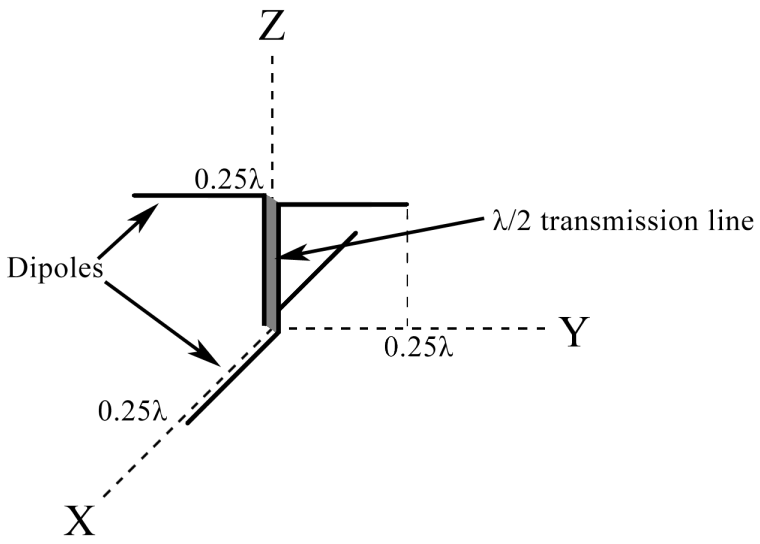

Figure 17: Geometry of a Tilston cell. The figure depicts an LHCPSS (assuming the wave is travelling in the positive z-direction).

If a circularly polarized wave illuminates the LHCPSS Tilston cell as seen in Figure 17 at normal incidence its linear components will be picked up by the dipoles causing voltages over the central gaps. If the incoming wave was LHCP then the voltages are in phase, that is if there is a positive voltage on one end of the transmission line there will also be one on the other end. If the incoming wave was RHCP the voltages would be out of phase instead.

If the cell is illuminated by an LHCP wave and the voltages are in phase, there will be a symmetry around the transmission line. From each side, it will appear as if the transmission line was half as long and the wave had been positively reflected at the center, the same as if there was an open-circuit. A quarter-wavelength transmission line transforms an open-circuit into a short-circuit, which is what will be seen at the feed of the dipoles. The two dipoles are then in resonance and will radiate an LHCP wave, as with the Pierrot cell, adding out of phase with the transmitted wave leaving only an LHCP polarized reflected wave.

For an input RHCP wave the voltages will instead be out of phase. Similar to

the thinking with the LHCP wave, the midpoint of the transmission line will now appear to be a short-circuit which is transformed through the quarter-wavelength transmission line into an open-circuit at the feed of the dipoles. With an open circuit there is no current at the center of the dipoles and they are not in resonance, hence they will not radiate and the RHCP wave will be transmitted through the structure unimpeded.

It is important to note that the transmission line must have an electrical length of a half-wavelength in order to properly transform the open- and short-circuits, but at the same time have a physical length of a quarter-wavelength in order to ensure the dipoles pick up the orthogonal components in phase. In the original design this was achieved by using a dielectric material to enclose the transmission line.

3.1.3 Morin

The final design was introduced by Morin [11] and is different from the other two in that each of the cells are interconnected forming a long helix like structure as can be seen in Figure 18.

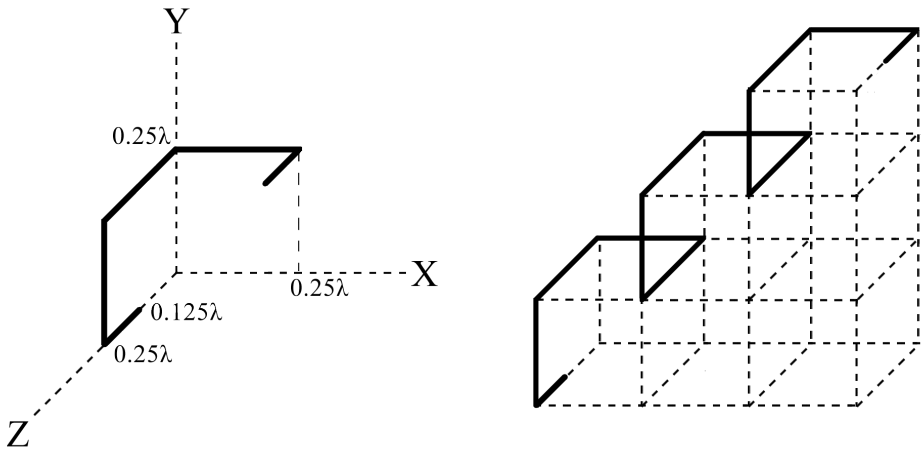

Figure 18: On the left is the geometry of an RHCPSS Morin cell, each side of the cube it borders is a quarter-wavelength long. On the right several interconnected cells can be seen forming a helix.

The design is similar to the previous designs in that two transverse portions are separated by a quarter-wavelength. Looking at the interconnected RHCPSS on the left in Figure 18, when it is illuminated at normal incidence by an RHCP wave currents will be induced on the transverse parts. The currents on the two

different parts will be out of phase due to the turn of the wire. However, when the current from the center of the top layer reaches the center of the bottom layer, it has travelled a distance of a half-wavelength and as such it adds in phase with the other induced current.

As the currents add in phase the wire will be in resonance and fields will be radiated. Waves from the top wire will travel $\frac{\lambda}{4}$ to reach the lower wire and waves radiated from the lower wire are already $\frac{\lambda}{2}$ out of phase, giving a total phase difference of $\frac{3\lambda}{4}$, resulting in an RHCP wave, which just as in the other two cases is out of phase with the original transmitted wave leaving only a reflected RHCP polarized wave.

If the CPSS is instead illuminated by an LHCP wave the induced currents will be in phase at first, but then add out of phase due to the half-wavelength distance. As the currents add out of phase, there will be no current flowing and the structure appears transparent.

Compared to the other two designs, the Morin helix has an advantage in that each cell is interconnected. As such it would be possible to hold it up by attaching the side of the helix in a frame. The other two cells are supposed to float freely in space, so while the Pierrot cell does not include any dielectric materials in its design, in order to realize it in practice each cell would have to be held in place by some sort of dielectric material.

3.2 Implementations

The designs explained in the previous subsection are relatively simple theoretical ones with well motivated dimensions. When implementing these designs for simulations, those dimensions might change as a result of optimization, and also other dimensions not mentioned in the previous text may need to be specified. The exact parameter dimensions that lead to the best performance will be presented in Section 5, however in this subsection the structures as they were prepared for the simulation are presented. Some of the designs are more or less direct implementations of the theoretical one, however others provide a slightly different take on the same base ideas. One trait that is shared among all of the designs is that the thickness of the wire must be specified. While there is no maximum value, as stated in Section 2.5 there is a minimal requirement of at least a diameter of 0.2 mm.

The dimensions seen in the figures do not necessarily represent fully optimized parameter values and are in some cases chosen specifically to highlight the shape of the structure.

3.2.1 Pierrot

The Pierrot cell is the simplest of the designs and as such no major changes has been suggested for it. The implemented design can be seen in Figure 19. The main new parameters that need to be specified are the separation between the unit cells in both x- and y-direction. There are no theoretical values for these parameters however it is common to set them around $\frac{\lambda}{2}$ for unit cell structures.

Another thing to notice is the orientation of the cells. As can be seen, particularly in the right figure, they are placed at a 45° angle. The theoretical design does not specify how the individual unit cells should be oriented to each other, however putting it at an angle allows for the possibility of grouping the cells closer together (as can be seen in Figure 19 where the unit cells are partially overlapping).

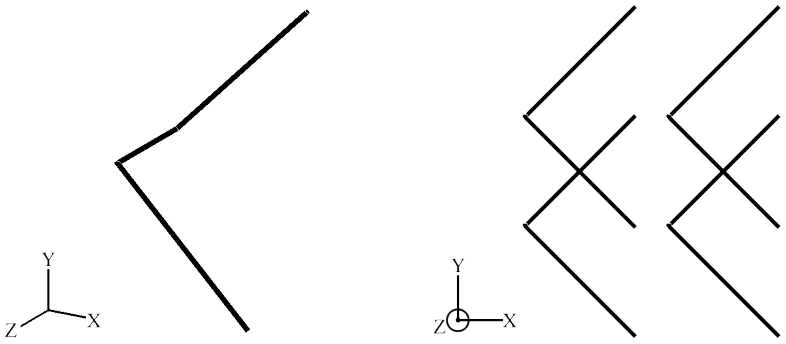

Figure 19: A view of the Pierrot unit cell and the full structure.

3.2.2 Tilston

With the Tilston cell, the main idea is that the center piece connecting the two dipoles has an electrical length of a half-wavelength but a physical height of a quarter-wavelength. The theoretical design suggested a $\frac{\lambda}{2}$ transmission line, which can be achieved using a dielectric. This implementation can be seen in Figure 20.

The most interesting new parameter to specify is the relative permittivity of the dielectric material (theoretically, $\varepsilon_r = 4$ gives an electrical length twice as long as the physical one). However, the diameter of the dielectric cylinder as well as the separation of the two wires going inside it also need to be specified.

As an alternative implementation, instead of using a dielectric to achieve the difference in electrical and physical length, a helical structure can be used. An

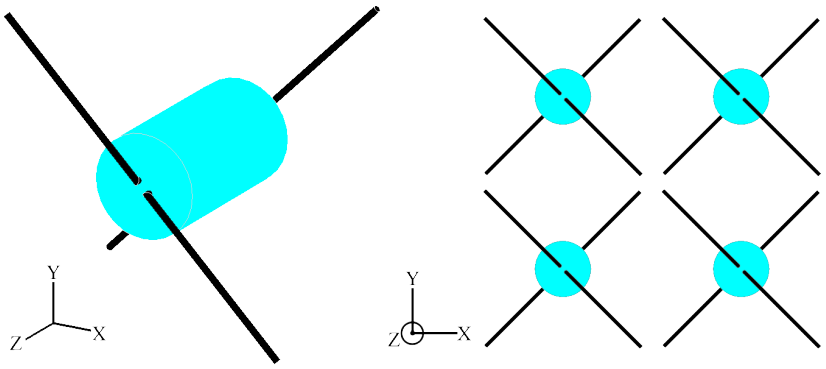

Figure 20: A view of the Tilston unit cell and the full structure.

implementation of this idea, henceforth referred to as a Helical Tilston, can be seen in Figure 21.

Compared to the dielectric implementation the difference is that instead of using a dielectric cylinder to realize the transmission line, the two wires connecting the dipoles instead form a double helix such that the length of the wires is twice the height of the helix. A new parameter that needs to be specified is the amount of turns of the helix. Note that due to the geometry, the amount of turns cannot be an even integer as the two dipoles would not properly connect then. For RHCPSS a quarter of a turn need to be added (for example, 5.25 turns) while for LHCPSS three quarters of a turn should be added (for example, 5.75 turns). The diameter of the helix also need to be specified. As the main requirement is that the wire length is twice as long as the height, these two parameters can theoretically not be entirely freely chosen.

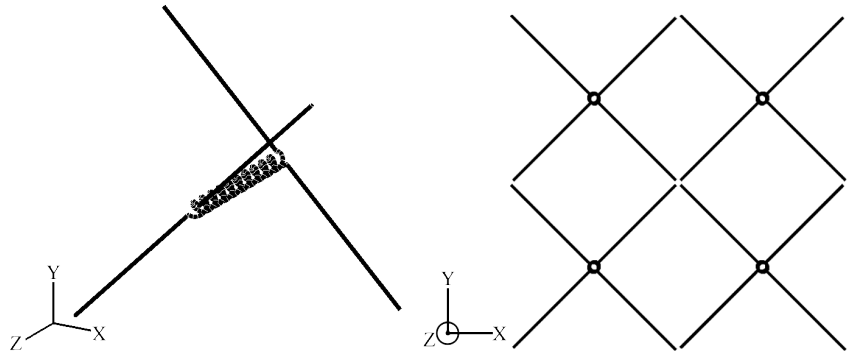

Figure 21: A view of the helical Tilston unit cell and the full structure.

Assuming that the number of turns is set at N, the helix diameter is D and the

total z-height of the helix is l_z, then the length of the wire is $\sqrt{(D\pi)^2 + \left(\frac{l_z}{N}\right)^2} \cdot N$. Since the length should be $2 \cdot l_z$, the diameter should be $D = \frac{\sqrt{3} \cdot l_z}{\pi N}$. Of course, as with the other parameters this can be changed by the optimization.

As with the Pierrot cell, both of these structures are placed at an angle to allow for more freedom in the unit cell size.

3.2.3 Morin

A standard implementation of the Morin cell can be seen in Figure 22 (called a Single Morin to differentiate from other Morin based designs). Unlike the Tilston and Pierrot designs, there is not complete freedom in choosing the cell sizes. If the transverse wire length is defined as l_{xy}, then in order for the unit cells to link together and form complete helices the separation in the x-direction (or whichever runs along the helices) need to be $\sqrt{2} \cdot l_{xy}$. The y-separation on the other hand can be set freely which allows the freedom to pack the helices very close together should this prove advantageous.

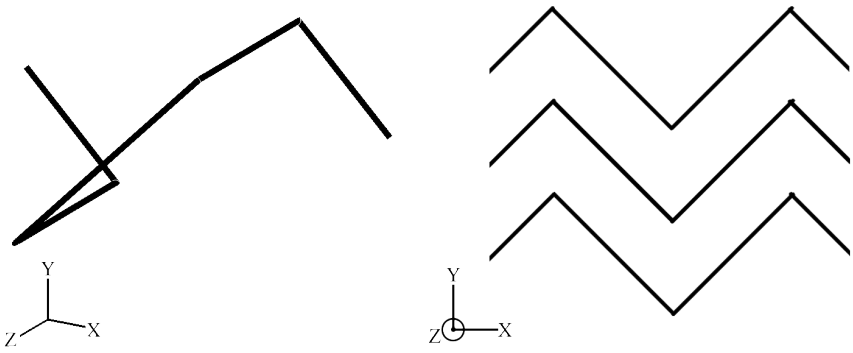

Figure 22: A view of the single Morin unit cell and the full structure where they form helices.

There are quite a few proposed adjustments to the Morin cell. The ideas behind the adjustments is to provide a denser pattern, which potentially can improve performance. A simple adjustment can be seen in Figure 23. In this design, called a Double Morin, the helices are differently aligned, creating an overall different pattern. Since the peaks of the helices (where the red and the black helix meet in the figure) are now potentially very close together (if the gap is made very small) it could be possible to attach the helices to each other using some form of dielectric material to improve structural stability. The effects of such a structure on the performance however has not been evaluated and as such it is purely a potential benefit.

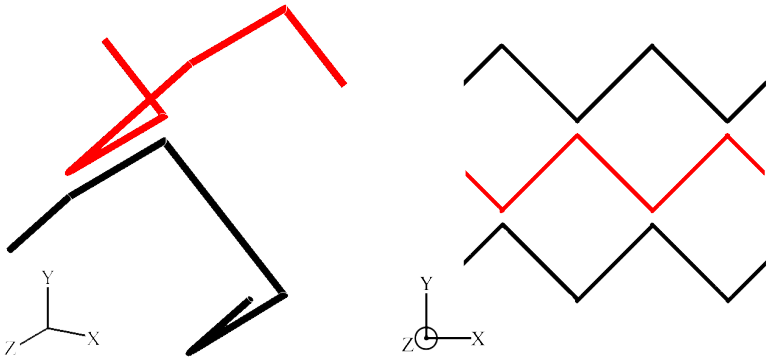

Figure 23: A view of a double Morin unit cell and the full structure.

A similar structure to the Double Morin can be achieved using a simpler unit cell as in Figure 24. The unit cell now looks similar to the Tilston design, hence it is called a Morin-Tilston. Functionally the Morin-Tilston works like a Morin cell and the similarity with the Tilston cell is purely aesthetic.

Compared to the Double Morin, the Morin-Tilston has a noticeably smaller and simpler unit cell, but the overall shape becomes very similar. However, while the two helices can be freely separated in the Double Morin, large separation is not possible with the Morin-Tilston or the connecting z-wire will get significantly bent.

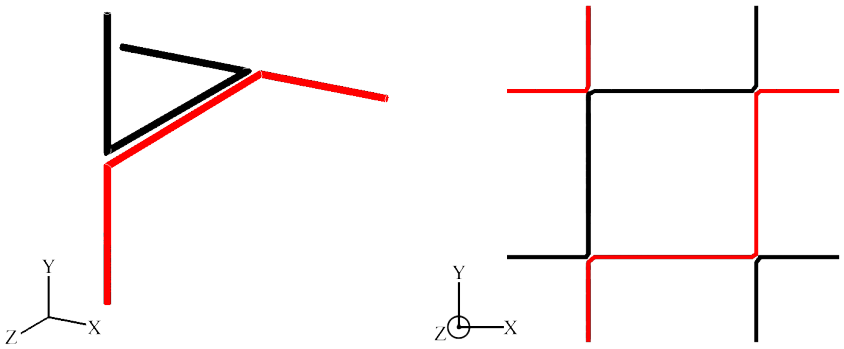

Figure 24: A view of a Morin-Tilston unit cell and the full structure.

The final variation on the Morin design can be seen in Figure 25. In this design, two helices cross each other at a 90° angle, thus it is called the Crossed Morin. The idea is that by crossing the helices they might provide a better coverage of the area and have better performance.

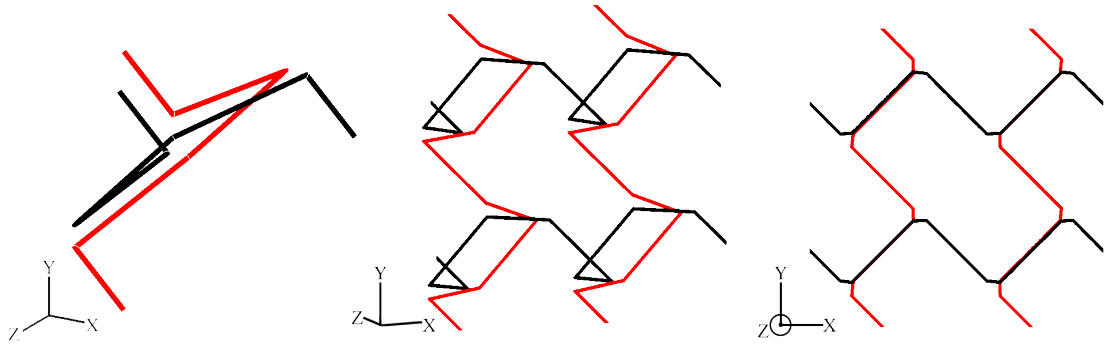

Figure 25: A view of crossed a Crossed Morin unit cell and the full structure.

4 Aim

The aim of the thesis is to examine and evaluate how suitable CPSS surfaces would be for creating a DGR equivalent for circular polarization. The main basis of the evaluation are requirements defined by the European Space Agency (ESA), but other goals include examining the structures for oblique incidence angles. The requirements have previously been stated in Section 2.5 but are repeated below:

- **IL** $\leq 0.5\,\mathrm{dB}$
- **RL** $\leq 0.5\,\mathrm{dB}$
- **AR** $\leq 0.75\,\mathrm{dB}$
- *IL, RL and AR bandwidth should be as wide as possible*
- *The structures should be examined at up to* $30°$ *angle of incidence*
- *The structures should be able to handle at least* $10°$ *variance in angle of incidence*
- *The structures will be designed for operation at* $10\,\mathrm{GHz}(\lambda = 30\,\mathrm{mm})$ *and simulated for* $8 - 12\,\mathrm{GHz}$
- *The wire diameter, a, must be at least* $0.2\,\mathrm{mm}$

5 Simulations

The simulations were made using CST (as described in Section 2.6) and the general process was to first recreate the design with parameters as close to the theoretical values as possible under normal incidence. When the design had been successfully modelled each parameter was manually changed in order to give an idea of how the parameters affected the performance. When the effect of the parameters were more well understood a rough manual attempt at optimizing the performance was made before eventually using CST's internal optimization tool to optimize the design. All of the design work and optimization was done for normal incidence.

The optimization goals used were the IL, RL and AR requirements specified above. While the structures were simulated for 8-12 GHz if the optimization ran over the entire range it was sometimes found that the optimum parameters were such that the IL, RL and AR did not overlap (for example, the RL might be centered at 10.5 GHz while the AR at 11 GHz), in order to prevent this the optimizer was limited to only operate between 9 and 11 GHz.

Once the design was optimized it was also tested for oblique incidence with angles of 5°, 10°, 20° and 30°. When simulating some of the structures at oblique angles it was found that the performance was not symmetrical (the response was not the same when going from port 1 to port 2 as it was for port 2 to port 1). It was discovered that each of the structures have certain incidence planes where they are symmetrical for oblique incidence, most likely caused by a lack of structural symmetry between the two directions although it is difficult to see from just visually analysing the structures.

In this section the result for each of the designs previously explained in section 3 is presented for normal incidence, as well as which incidence planes gives symmetrical responses and the results of oblique incidence for these planes. The results will consist of the IL, RL and AR as well as the physical parameters of the optimized unit cells.

The simulation is set up with two ports on each side of the structure with waves travelling between them. The structures simulated are RHCPSS's and for the results only the relevant graphs are shown. That is, for an RHCPSS only the RHCP return loss and the LHCP insertion loss are shown.

The parameter dimensions presented in this section are taken from the optimization and presented at a relatively high accuracy which is probably not achievable if the structures were to be physically realized. After some testing with the simulation it appears that rounding the parameters to a 0.1 mm accuracy appears to only marginally affect the performance.

5.1 Normal Incidence

5.1.1 Pierrot

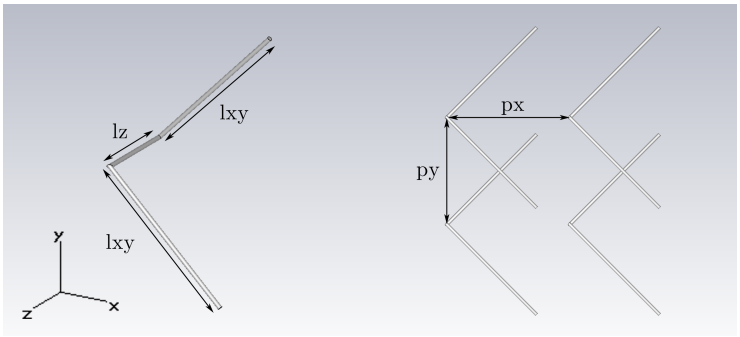

Figure 26: The Pierrot cell with all variable parameters specified.

The structure can be seen in Figure 26. The best parameters were found as:

$$\begin{aligned} \mathbf{l_{xy}} &= 13.590\,\text{mm}\ (\approx 0.45\lambda) \\ \mathbf{l_z} &= 7.508\,\text{mm}\ (\approx 0.25\lambda) \\ \mathbf{p_x} &= 13.328\,\text{mm}\ (\approx 0.44\lambda) \\ \mathbf{p_y} &= 11.929\,\text{mm}\ (\approx 0.40\lambda) \\ \mathbf{a} &= 0.362\,\text{mm} \end{aligned}$$

Achieved bandwidth: 1.05 GHz (10.5%)

This resulted in the IL, RL and AR as can be seen in Figures 27.

The Pierrot cell is generally bandwidth limited by the AR. The center of the AR is in turn almost entirely determined by the l_z height as long as the other parameters don't vary too much. The bandwidth of the AR is also quite difficult to improve, as it is barely affected by the other parameters. Improving the IL and RL is more easily achieved.

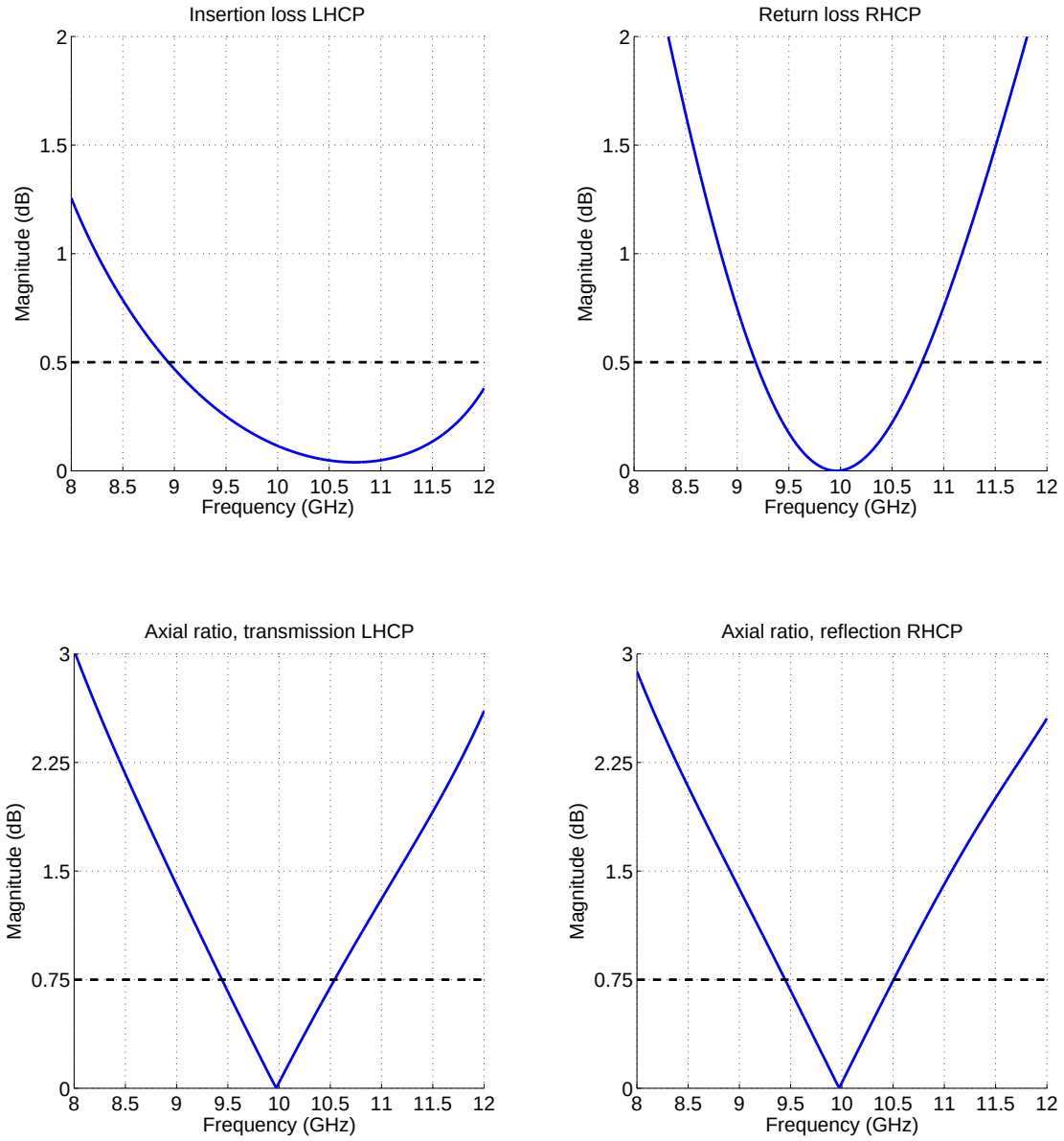

Figure 27: IL, RL and AR for an RHCPSS Pierrot structure at normal incidence.

5.1.2 Tilston

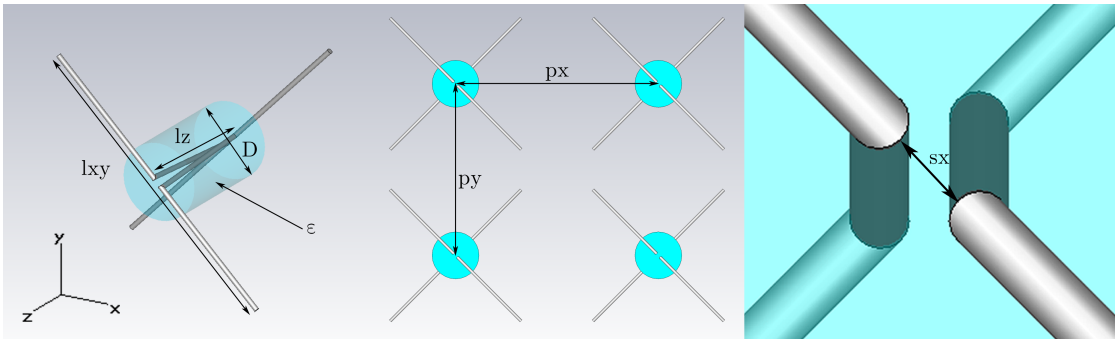

Figure 28: The Tilston cell with all variable parameters specified.

The structure can be seen in Figure 28. The best parameters were found as:

$$\begin{aligned}
\mathbf{l_{xy}} &= 16.399\,\text{mm}\ (\approx 0.55\lambda)\\
\mathbf{l_z} &= 7.121\,\text{mm}\ (\approx 0.24\lambda)\\
\mathbf{p_x} &= 12.469\,\text{mm}\ (\approx 0.42\lambda)\\
\mathbf{p_y} &= 12.529\,\text{mm}\ (\approx 0.42\lambda)\\
\mathbf{D} &= 3.934\,\text{mm}\\
\mathbf{s_x} &= 0.693\,\text{mm}\\
\mathbf{a} &= 0.257\,\text{mm}\\
\boldsymbol{\varepsilon} &= 4.267
\end{aligned}$$

Achieved bandwidth: 0.83 GHz (8.3%)

Note that while the z-height of the dielectric cylinder is not marked, it is the same as l_z.

The IL is quite good, as is the RL. The AR has a slightly lower bandwidth than the Pierrot cell which means that overall the performance is slightly worse.

As before, the center of the AR can be set by the l_z length while the IL and RL depend more on the l_{xy} length. The relative permittivity, ε, generally affects both the RL, IL and the AR however it can be counteracted by the l_z and l_{xy} parameters. As such, if the permittivity cannot be freely chosen to any value desired, it is possible to design the rest of the structure around the available material. The p_x and p_y lengths affects primarily the IL and RL, with a smaller unit cell resulting in a higher RL and a lower IL.

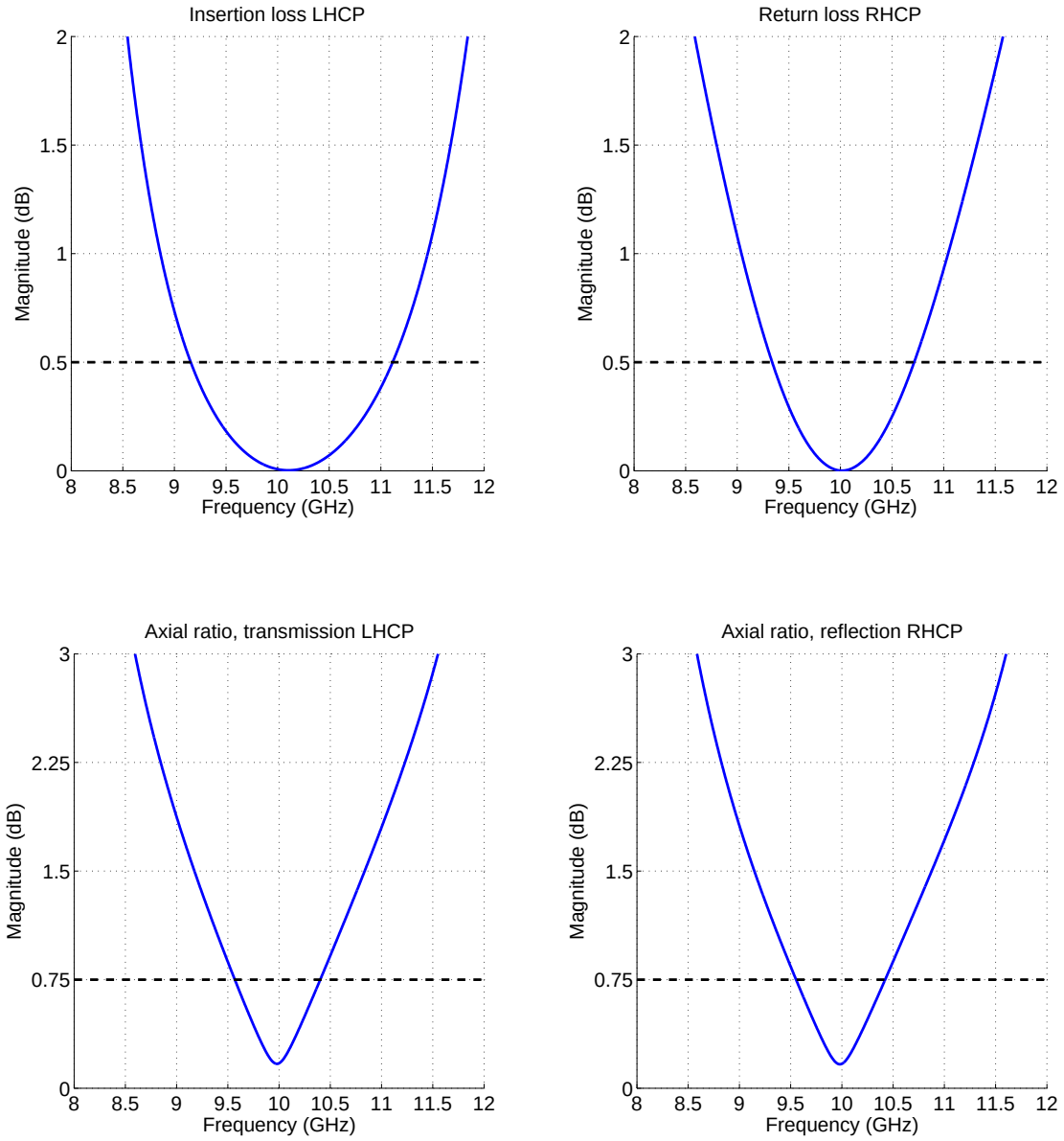

Figure 29: IL, RL and AR for an RHCPSS Tilston structure at normal incidence.

5.1.3 Helical Tilston

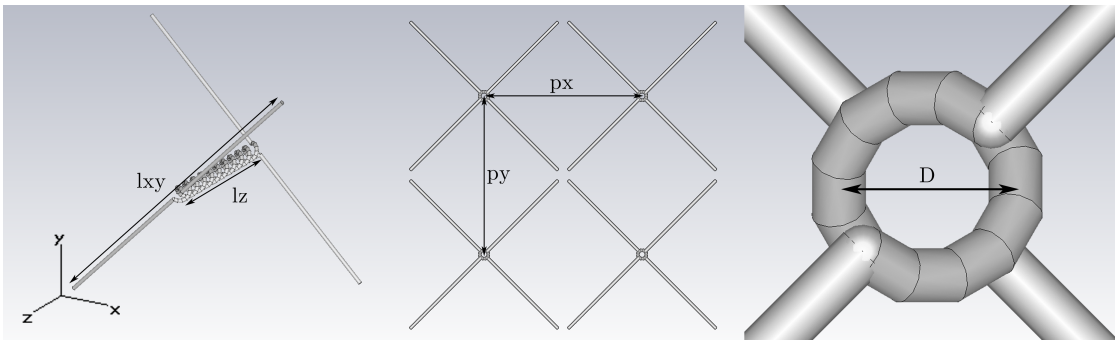

Figure 30: The Helical Tilston cell with all variable parameters specified.

The structure can be seen in Figure 30. The best parameters were found as:

$$\begin{aligned}
\mathbf{l_{xy}} &= 16.392\,\text{mm}\ (\approx 0.55\lambda) \\
\mathbf{l_z} &= 7.500\,\text{mm}\ (\approx 0.25\lambda) \\
\mathbf{p_x} &= 11.892\,\text{mm}\ (\approx 0.40\lambda) \\
\mathbf{p_y} &= 11.870\,\text{mm}\ (\approx 0.40\lambda) \\
\mathbf{N} &= 5.25 \\
\mathbf{R} &= 0.674\,\text{mm}\ (\approx 0.86 \cdot \frac{\sqrt{3} \cdot l_z}{\pi \cdot N}) \\
\mathbf{a} &= 0.2\,\text{mm}
\end{aligned}$$

Achieved bandwidth: 1.08 GHz (10.8%)

The AR bandwidth is improved slightly compared to the dielectric implementation of the Tilston cell while the RL is similar. As usual, the l_z length mainly determines the center of the AR bandwidth while the l_{xy} length the RL. The amount of turns, N, mainly affects the AR with a higher amount of turns giving better performance, although there are diminishing returns and eventually adding more turns does not change performance much.

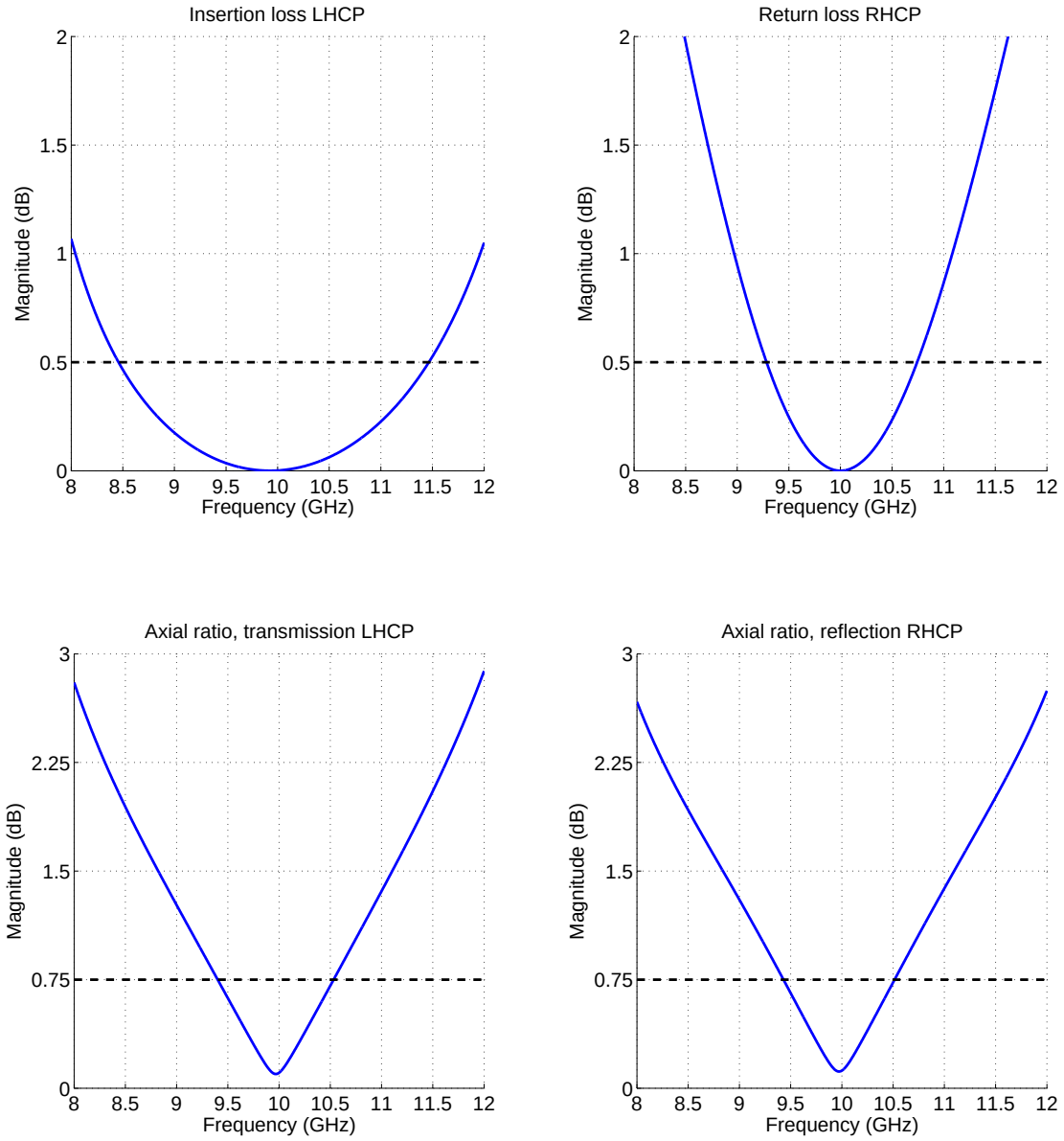

Figure 31: IL, RL and AR for an RHCPSS Helical Tilston structure at normal incidence.

5.1.4 Single Morin

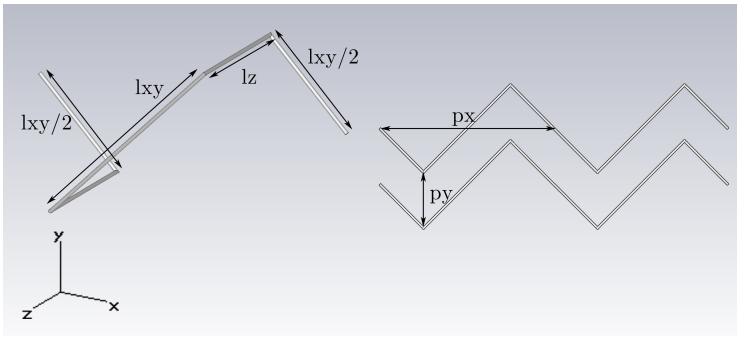

Figure 32: The Single Morin cell with all variable parameters specified except for the wire diameter, a, which is defined the same as for the other structures.

The structure can be seen in Figure 32. The best parameters were found as:

$$\begin{aligned} \mathbf{l_{xy}} &= 14.360\,\text{mm}\ (\approx 0.48\lambda) \\ \mathbf{l_z} &= 7.500\,\text{mm}\ (\approx 0.25\lambda) \\ \mathbf{p_x} &= 20.308\,\text{mm}\ (\sqrt{2}\cdot l_{xy}) \\ \mathbf{p_y} &= 4.062\,\text{mm}\ (0.2\cdot\sqrt{2}\cdot l_{xy}) \\ \mathbf{a} &= 0.245\,\text{mm} \end{aligned}$$

Achieved bandwidth: 1.04 GHz (10.4%)

The Single Morin cell has relatively decent bandwidth with over 1 GHz for the AR. In order to increase the RL bandwidth the helices are placed very close together, which is also the cause of the odd shape of the IL. The l_{xy} length is almost twice what it should theoretically be, this is because normally the peak of the AR and the RL do not overlap, but by adjusting the l_{xy} length it is possible to adjust the center of the RL with minimal effect on the AR. As previously, the center of the AR bandwidth is almost entirely determined by the l_z length.

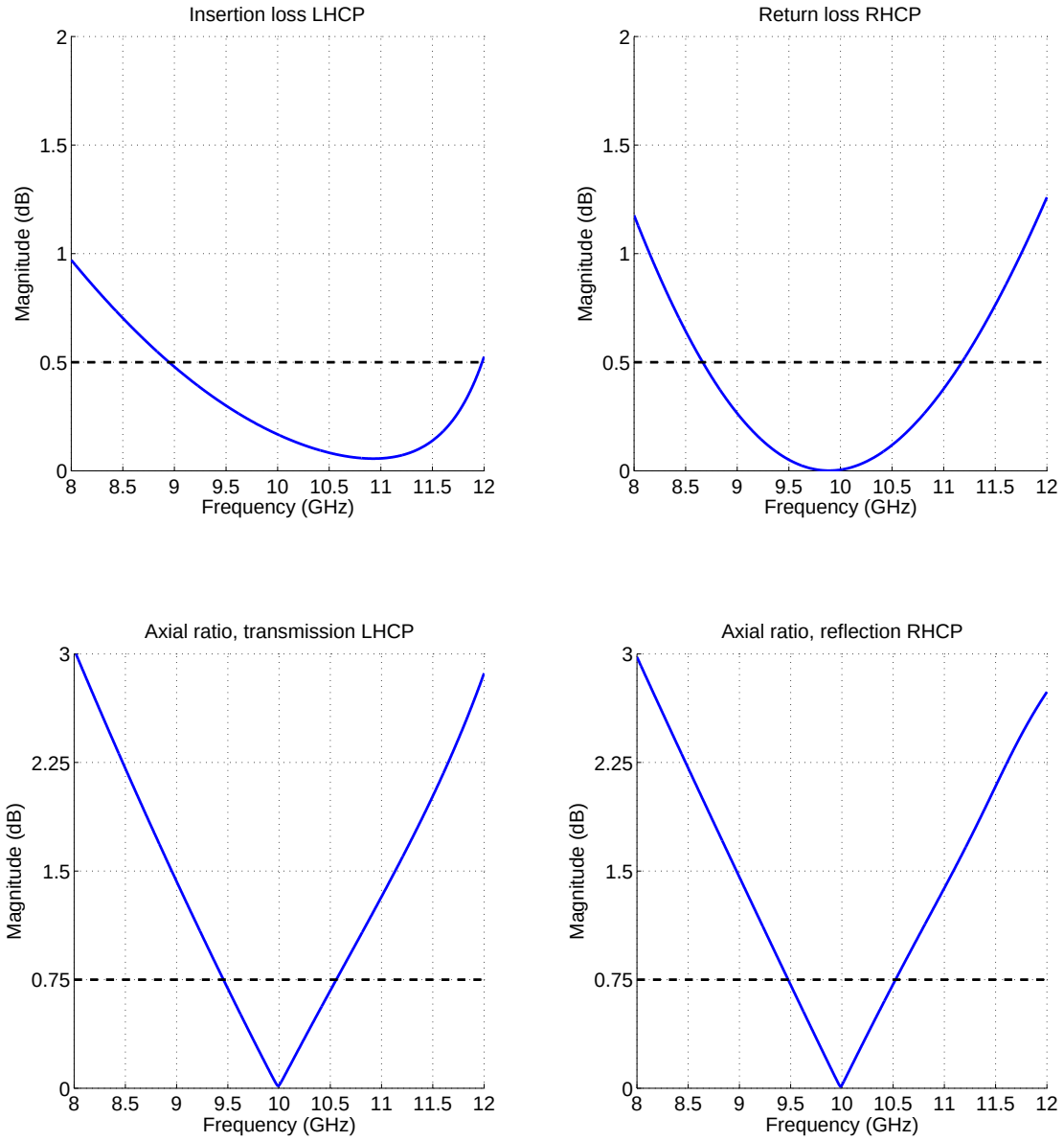

Figure 33: IL, RL and AR for an RHCPSS Single Morin structure at normal incidence.

5.1.5 Double Morin

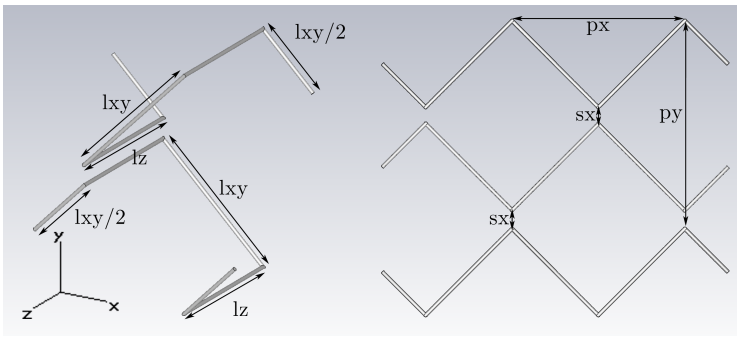

Figure 34: The Double Morin cell with all variable parameters specified.

The structure can be seen in Figure 34. The best parameters were found as:

$$\begin{aligned}
\mathbf{l_{xy}} &= 7.814\,\text{mm}\ (\approx 0.26\lambda) \\
\mathbf{l_z} &= 7.500\,\text{mm}\ (\approx 0.25\lambda) \\
\mathbf{s_x} &= 1.050\,\text{mm}\ (0.035\lambda) \\
\mathbf{p_x} &= 11.051\,\text{mm}\ (\sqrt{2}\cdot l_{xy}) \\
\mathbf{p_y} &= 13.151\,\text{mm}\ (\sqrt{2}\cdot l_{xy} + 2\cdot s_x) \\
\mathbf{a} &= 0.2\,\text{mm}
\end{aligned}$$

Achieved bandwidth: 0.98 GHz (9.8%)

The Double Morin has comparable performance to the Single Morin for normal incidence. As usual the AR is the limiting factor. The l_z length is pretty much the only factor determining the center of the AR bandwidth, while the l_{xy} length can be used to adjust the RL bandwidth so that it overlaps. The s_x size slightly affects the bandwidth of the AR slightly, however it does not affect both equally. A smaller s_x leads to a larger transmission bandwidth but a smaller reflection bandwidth. Overall the changes in the AR caused by the s_x is quite small, as it mainly affects the IL and RL. A smaller s_x leads to worse IL performance (and due to the shape of the IL, it is possible to reach a point where it never goes below 0.5 dB) but a better RL bandwidth.

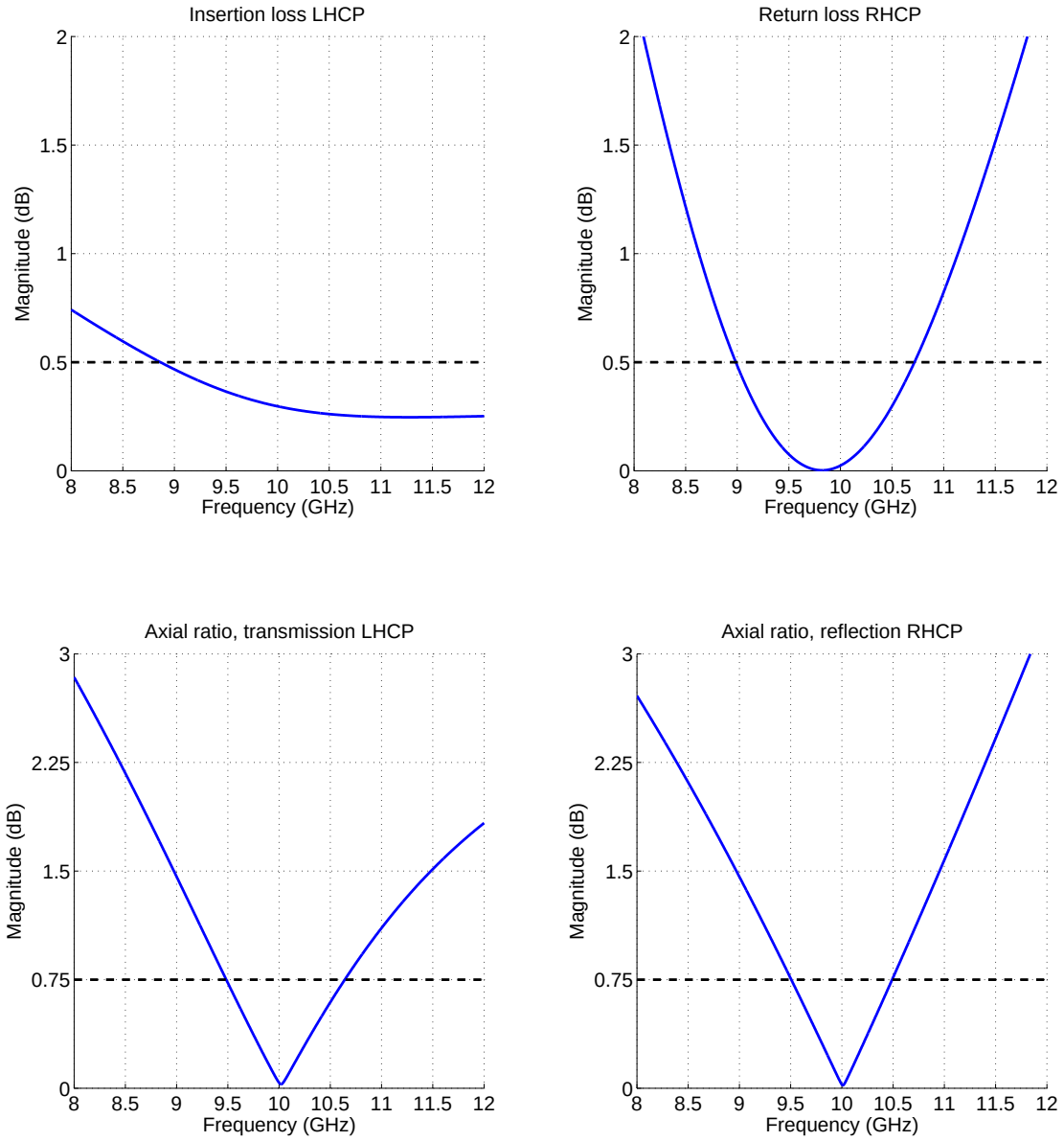

Figure 35: IL, RL and AR for an RHCPSS Double Morin structure at normal incidence.

5.1.6 Morin-Tilston

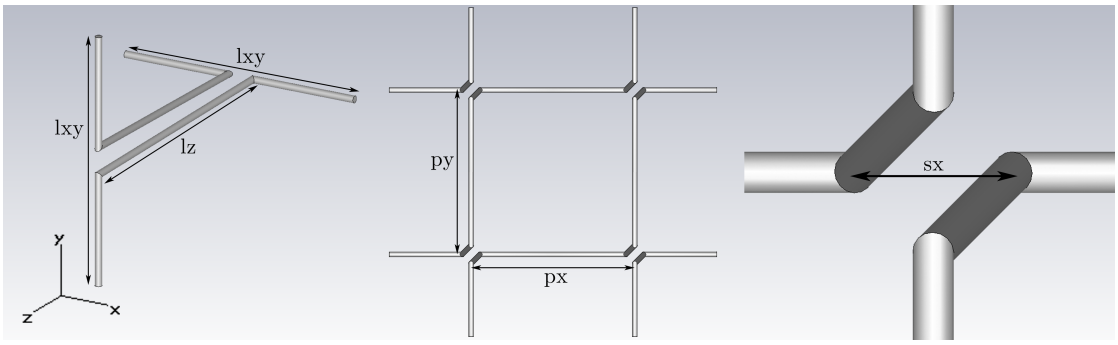

Figure 36: The Morin-Tilston cell with all variable parameters specified.

The structure can be seen in Figure 37. The best parameters were found as:

$$\begin{aligned}
\mathbf{l_{xy}} &= 7.000\,\text{mm}\ (\approx 0.23\lambda) \\
\mathbf{l_z} &= 7.500\,\text{mm}\ (\approx 0.25\lambda) \\
\mathbf{s_x} &= 0.774\,\text{mm}\ (0.026\lambda) \\
\mathbf{p_x} &= 7\,\text{mm}\ (l_{xy}) \\
\mathbf{p_y} &= 7\,\text{mm}\ (l_{xy}) \\
\mathbf{a} &= 0.2\,\text{mm}
\end{aligned}$$

Achieved bandwidth: N/A

No working design was found for the Morin-Tilston structure. Despite having a very similar structure to the Double Morin it appears that the changes made to create a smaller unit-cell is not necessarily a worthwhile trade-off.

However, in [7] a version of the Morin-Tilston was presented. In this version, thinner wires than what was allowed here was used and the structure was held up by having it rest on a dielectric foam. There is also a small hole in the foam around the vertical wires (like an inverted Tilston, with a dielectric material everywhere but around the vertical wires). With this type of structure the Morin-Tilston in [7] performs in line with the Double Morin (slightly worse, but the design presented is only marginally optimized).

This type of modified Morin-Tilston is not examined in this thesis, but seems to be a viable design. The Morin-Tilston as examined here however does not perform well enough to meet the requirements.

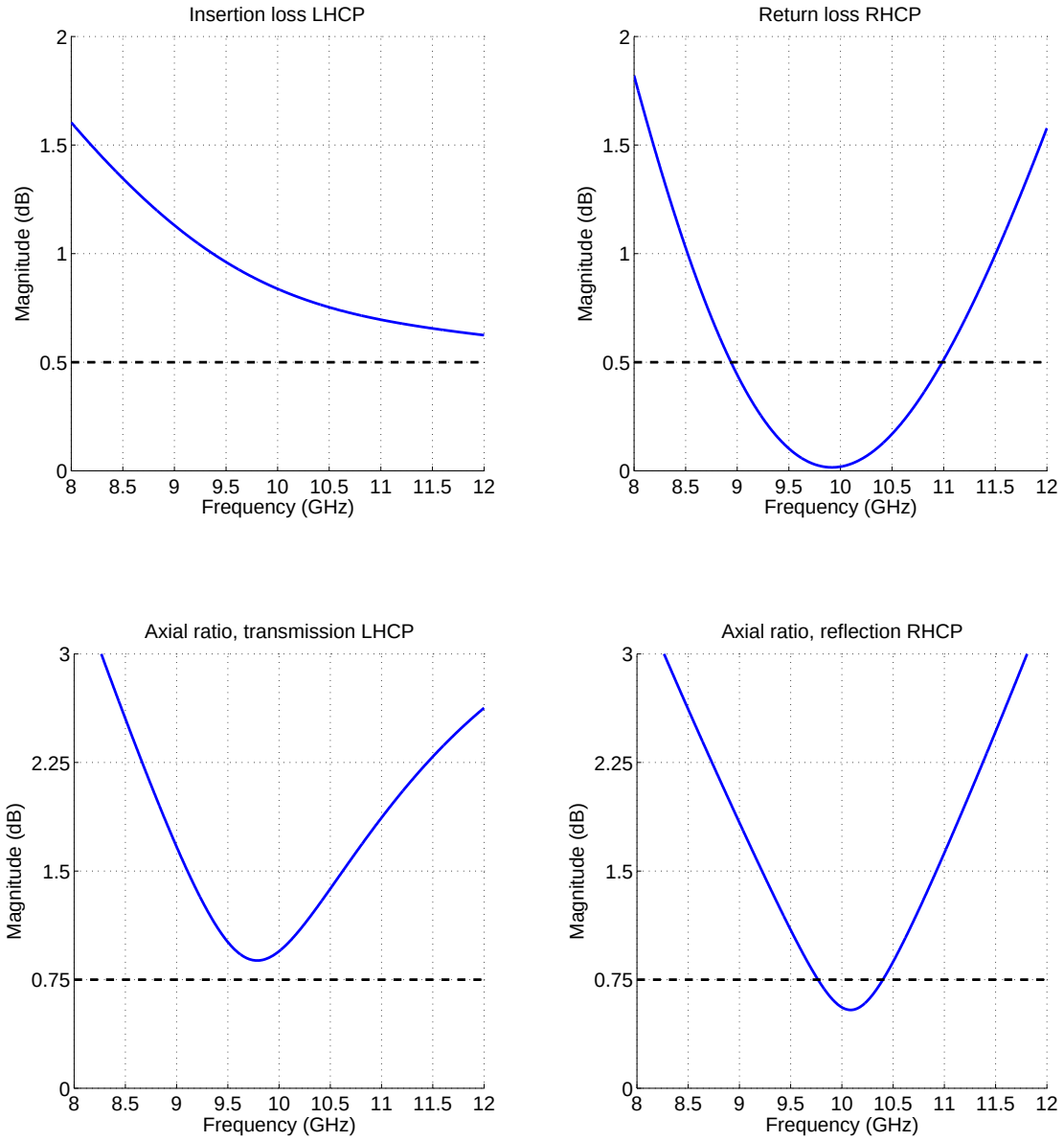

Figure 37: IL, RL and AR for an RHCPSS Morin-Tilston structure at normal incidence.

5.1.7 Crossed Morin

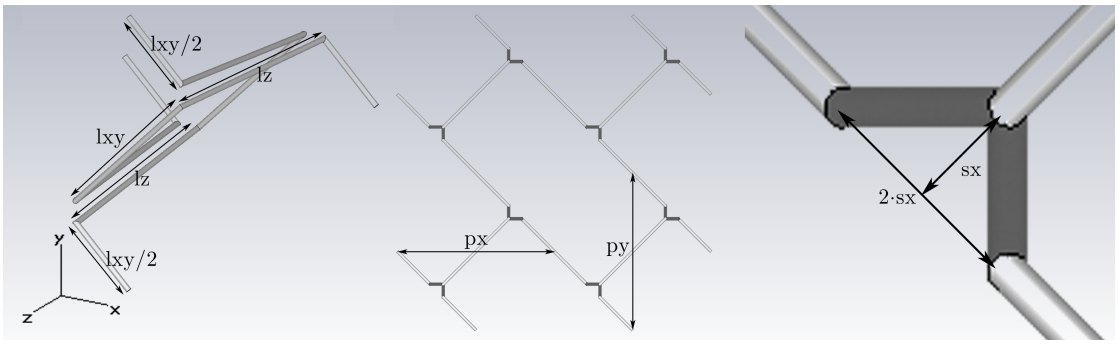

Figure 38: The Crossed Morin cell with all variable parameters specified.

The structure can be seen in Figure 38. The best parameters were found as:

$$\begin{aligned}
\mathbf{l_{xy}} &= 6.819\,\text{mm}\ (\approx 0.23\lambda) \\
\mathbf{l_z} &= 8.086\,\text{mm}\ (\approx 0.27\lambda) \\
\mathbf{s_x} &= 0.404\,\text{mm}\ (0.013\lambda) \\
\mathbf{p_x} &= 9.644\,\text{mm}\ (\sqrt{2}\cdot l_{xy}) \\
\mathbf{p_y} &= 9.644\,\text{mm}\ (\sqrt{2}\cdot l_{xy}) \\
\mathbf{a} &= 0.2\,\text{mm}
\end{aligned}$$

Achieved bandwidth: 0.89 GHz (8.9%)

The Crossed Morin design has slightly lower AR bandwidth than the Single and Double Morin designs but is comparable. The RL bandwidth on the other hand is significantly lower, however as the overall performance is still limited by the AR bandwidth this is not a significant issue.

The l_z length affects all of the measured parameters, and remains the main way to set the center of the AR bandwidth. The l_{xy} length primarily affects the IL and RL bandwidths and can be used to fine tune these parameters without greatly changing the AR. s_x also affects all of the parameters. The IL is generally higher when s_x is smaller, while the RL peak is mainly moved around. The AR is minimally affected by the s_x size.

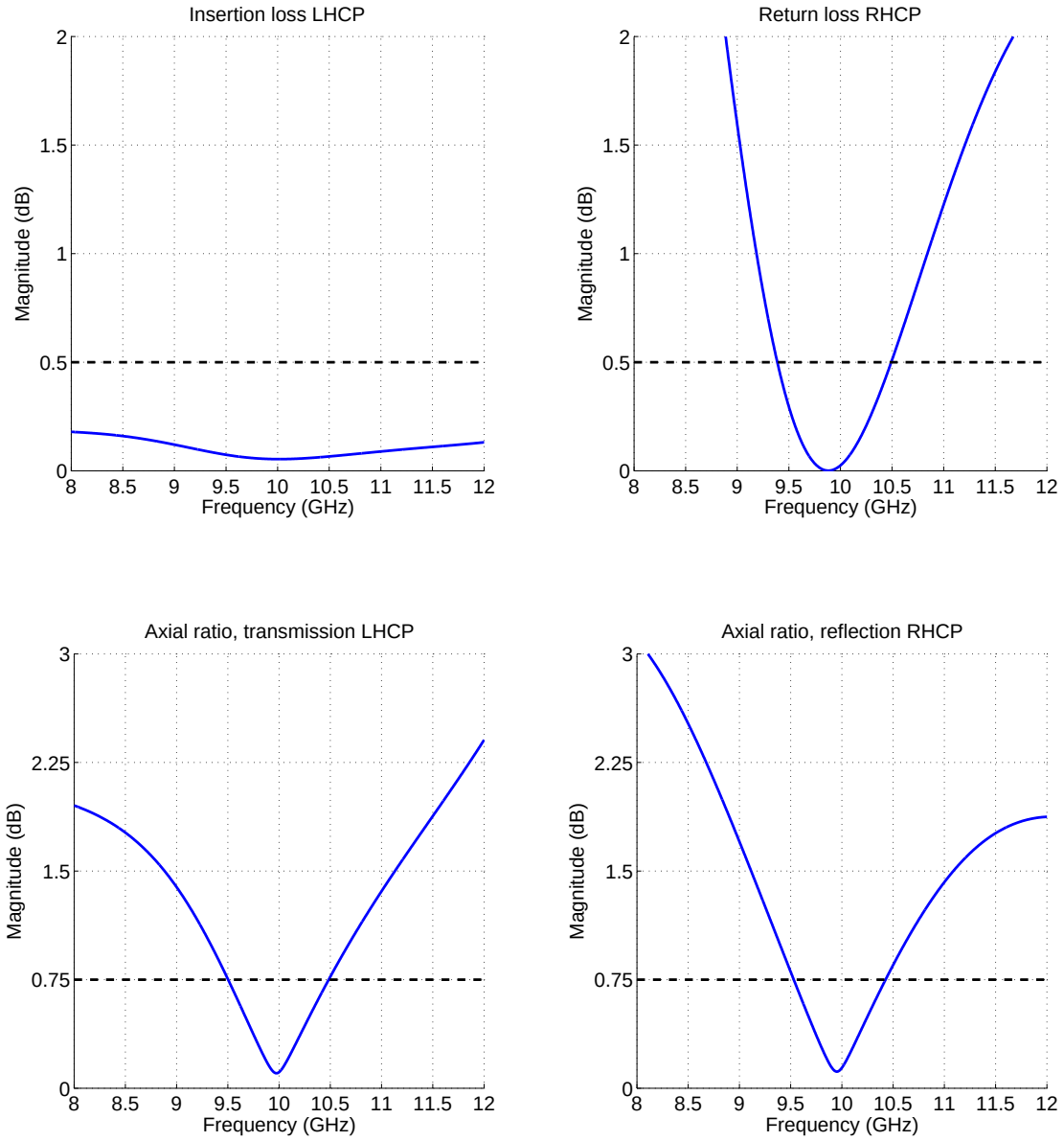

Figure 39: IL, RL and AR for an RHCPSS Crossed Morin structure at normal incidence.

5.1.8 Bandwidths

The achieved bandwidths for each of the structures are summarized below:

Design	Achieved bandwidth (GHz)
Pierrot	1.05
Tilston	0.83
Helical Tilston	1.08
Single Morin	1.04
Double Morin	0.98
Morin-Tilston	N/A
Crossed Morin	0.89

5.2 Incidence Plane

When the designs were tested for oblique incidence it was found that they only had symmetrical characteristics for certain incidence planes. An example of non-symmetrical behaviour can be seen in Figure 40 where the graphs should be identical for both directions but are clearly not. All of the designs were analyzed for various planes of incidence and the ones which gave symmetrical responses are marked in Figures 41-42. The performance for oblique incidence for these planes can be found in Section 5.3.

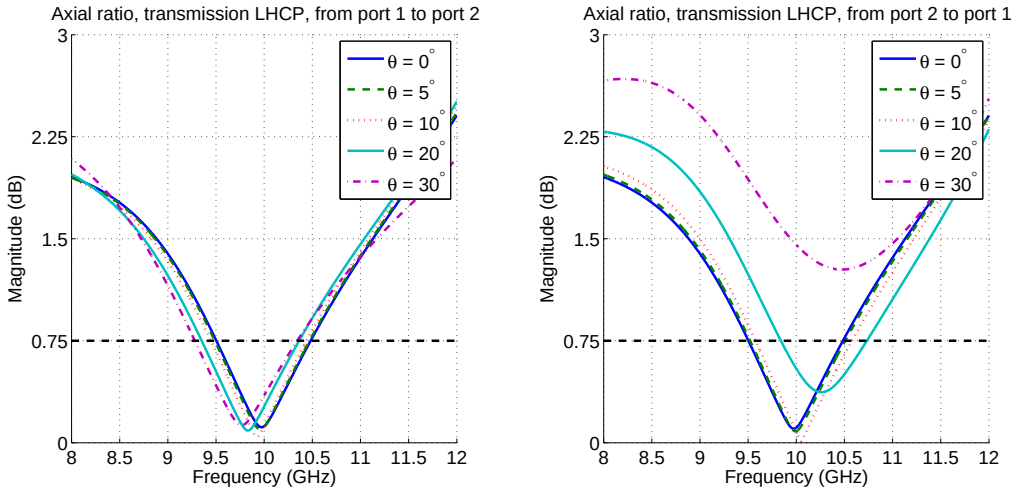

Figure 40: The non-symmetrical behaviour demonstrated for the Cross Morin structure in the $\varphi = 0$ plane.

The different planes will be named after which φ angle they are positioned at relative to the xz-plane as seen in Section 3.2 which the cells were designed for.

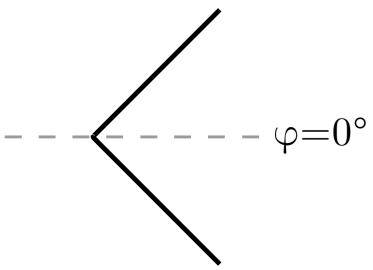

Figure 41: The only plane which gives symmetrical behaviour for the Pierrot cell is at $\varphi = 0°$.

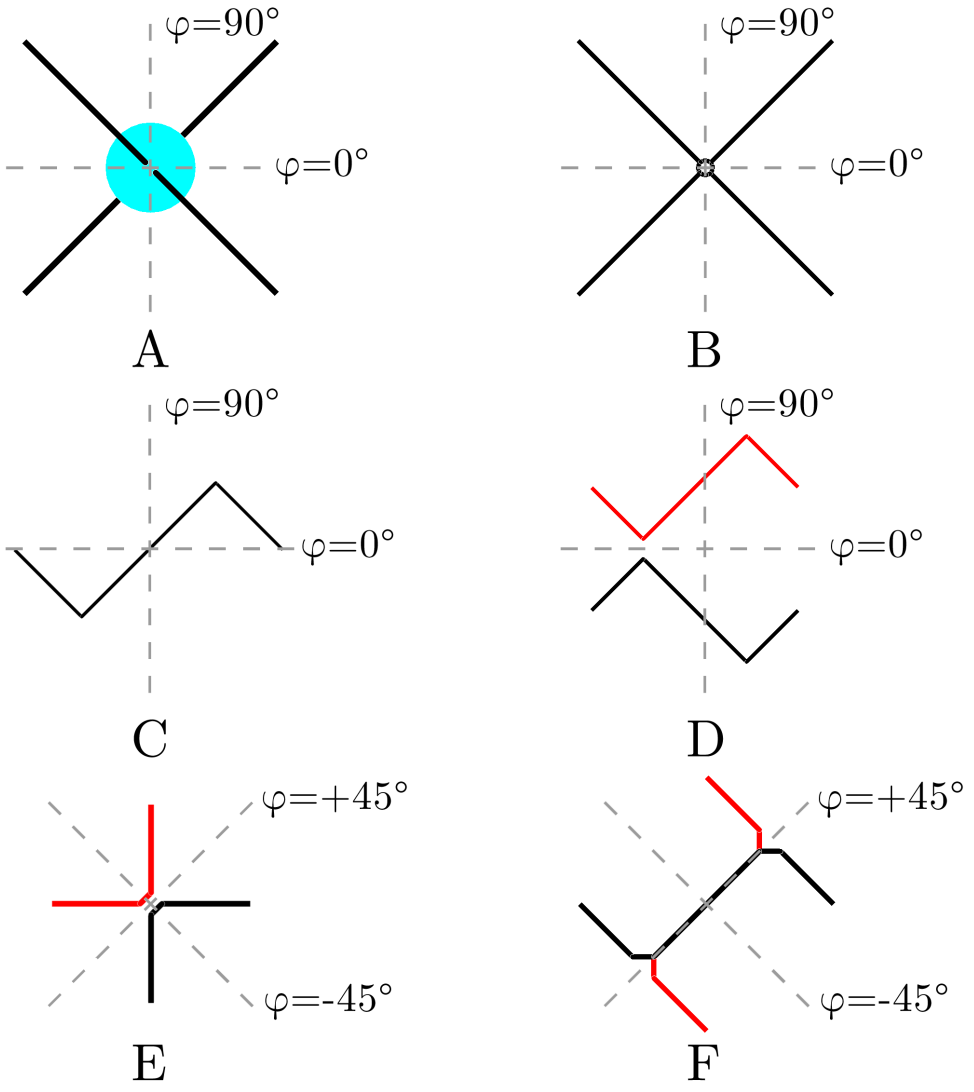

Figure 42: The various symmetrical incidence planes marked for the (A) Tilston, (B) Helical Tilston, (C) Single Morin, (D) Double Morin, (E) Morin-Tilston and (F) Crossed Morin designs.

5.3 Oblique Incidence

In this subsection the performance for different angles of incidence was recorded. The angle of incidence, θ, was changed while φ was held constant in one of the symmetrical planes found in the Section 5.2. The structures were simulated for θ values of $0°, 5°, 10°, 20°$ and $30°$. Note that for most of these structures the performance is identical for incidence at positive and negative values (for example, $\pm 10°$ is identical). This means that $-5°$ to $+5°$ will give a total span of $10°$. The Pierrot cell is the only one for which this is not the case, as such it is simulated for positive and negative angles of incidence.

5.3.1 Pierrot

The results can be seen in Figure 43. The Pierrot cell performs differently for positive and negative angles of incidence (although only for the AR). This demonstrates a lack of symmetry with respect to positive and negative angles of incidence in this plane, and means that one needs to think about which side the incoming waves are hitting in order to get the expected performance.

The impact on the IL and RL performance is minimal at up to $10°$ and could probably be manageable even at $20°$. The AR however experiences a strong frequency shift which means that even at $10°$ the impact is notable. A $0°$ to $\pm 10°$ or a $-5°$ to $+5°$ range could probably be manageable although with reduced AR bandwidth.

5.3.2 Tilston

The results can be seen in Figure 44. For both incidence planes the IL performance remains good even for very large angles of incidence. The RL on the other hand is largely unaffected at up to $10°$ and potentially manageable at $20°$ although it is starting to drift away.

For $\varphi = 0°$ the AR remains largely unaffected by the incidence angle at up to $10°$ and could be managed even at $20°$ although at this point the bandwidth would be decreased slightly from the shift in frequency. For $\varphi = 90°$ the AR starts to drift away already at $10°$ although not greatly. At $20°$ though it has drifted away quite a lot. The Tilston generally seems quite stable when it comes to incidence angle, especially for the $\varphi = 0°$ plane.

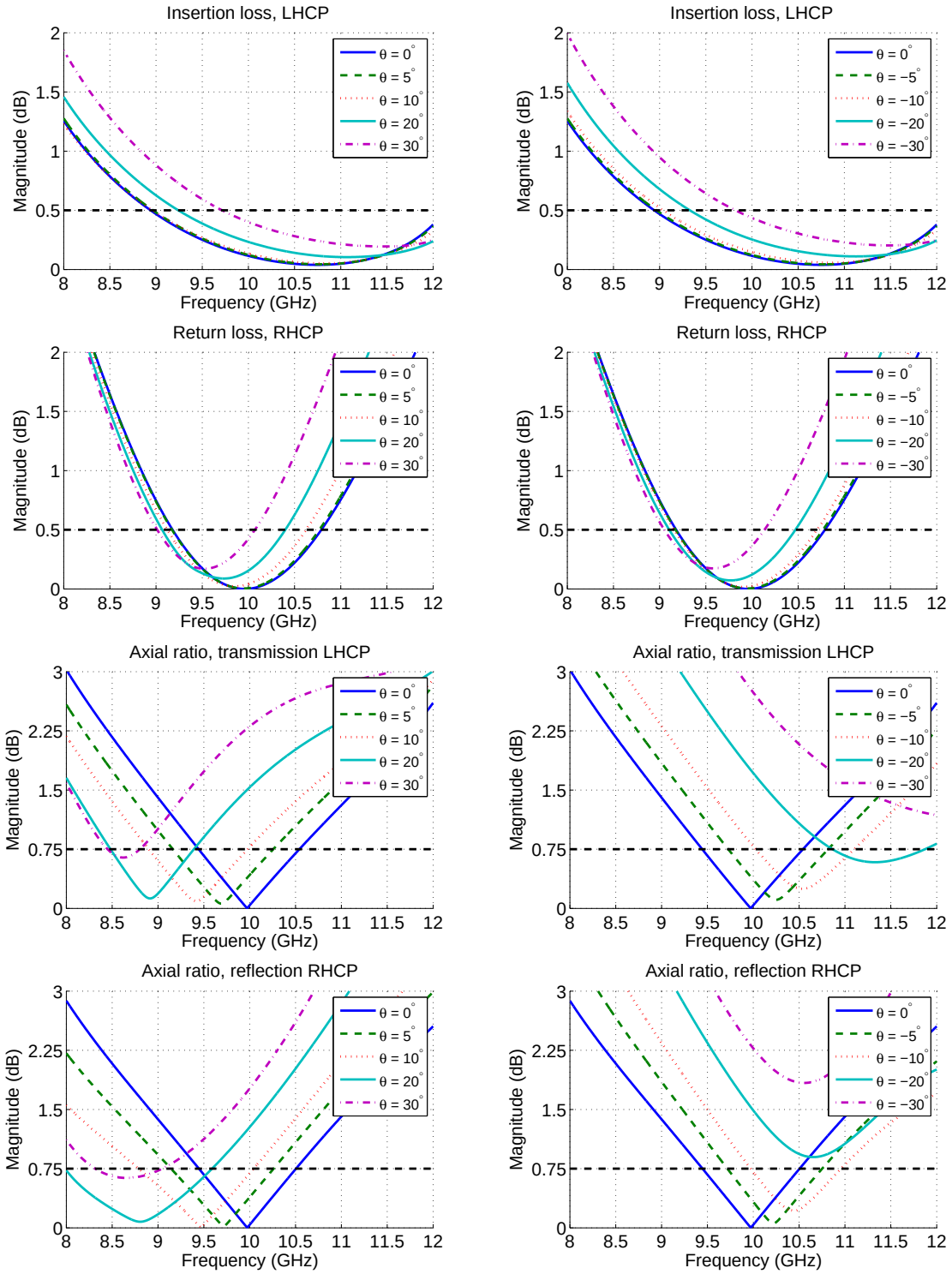

Figure 43: IL, RL and AR for an RHCPSS Pierrot structure at various angles of incidence in the $\varphi = 0°$ plane. Left: Positive angles, Right: Negative angles.

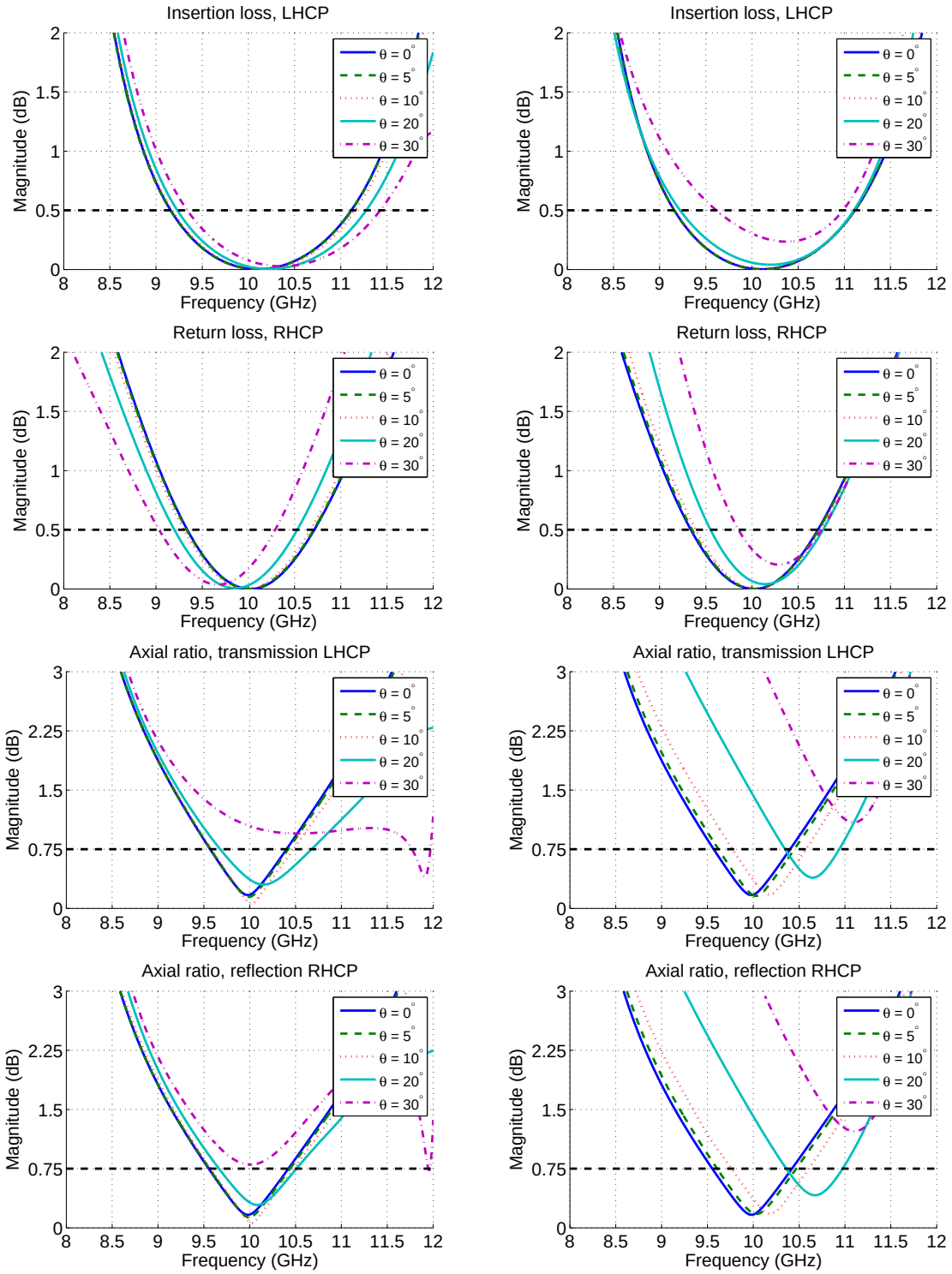

Figure 44: IL, RL and AR for an RHCPSS Tilston structure at various angles of incidence. Left:$\varphi = 0°$, Right: $\varphi = 90°$.

5.3.3 Helical Tilston

The results can be seen in Figure 45. For the $\varphi = 0°$ plane the effects on IL and RL are minimal up to 10° while for the $\varphi = 90°$ plane the RL does not start to drift away until 30°.

For the $\varphi = 90°$ plane the effects on the AR is minimal at up to 10° but at 20° it has already shifted away substantially. For the $\varphi = 0°$ plane the AR starts to drift slightly at 10° however with a reduced bandwidth it could still be manageable. Overall it has worse performance at higher angle of incidence than the dielectric Tilston implementation.

5.3.4 Single Morin

The results can be seen in Figure 46. The Single Morin does not perform particularly well for oblique angles in either plane and there appear to be several resonances that were not noticeable for normal incidence. It is possible that the cause of these resonances is the fact that the helices are significantly longer than what the theoretical models described (l_{xy} is almost twice as long as the theoretical model suggested). These longer helices might allow for more resonances than were previously not visible at normal incidence. As this extra length was necessary to achieve good performance at normal incidence, this could be a weakness of the Single Morin design.

5.3.5 Double Morin

The results can be seen in Figure 47. For both planes the performance impact is minimal at up to 10°. For the $\varphi = 0°$ plane the RL and AR has drifted noticeable in frequency at 20° however with a reduced bandwidth it could work. For the $\varphi = 90°$ plane however the AR bandwidth is so significantly reduced at 20° that it is probably unusable.

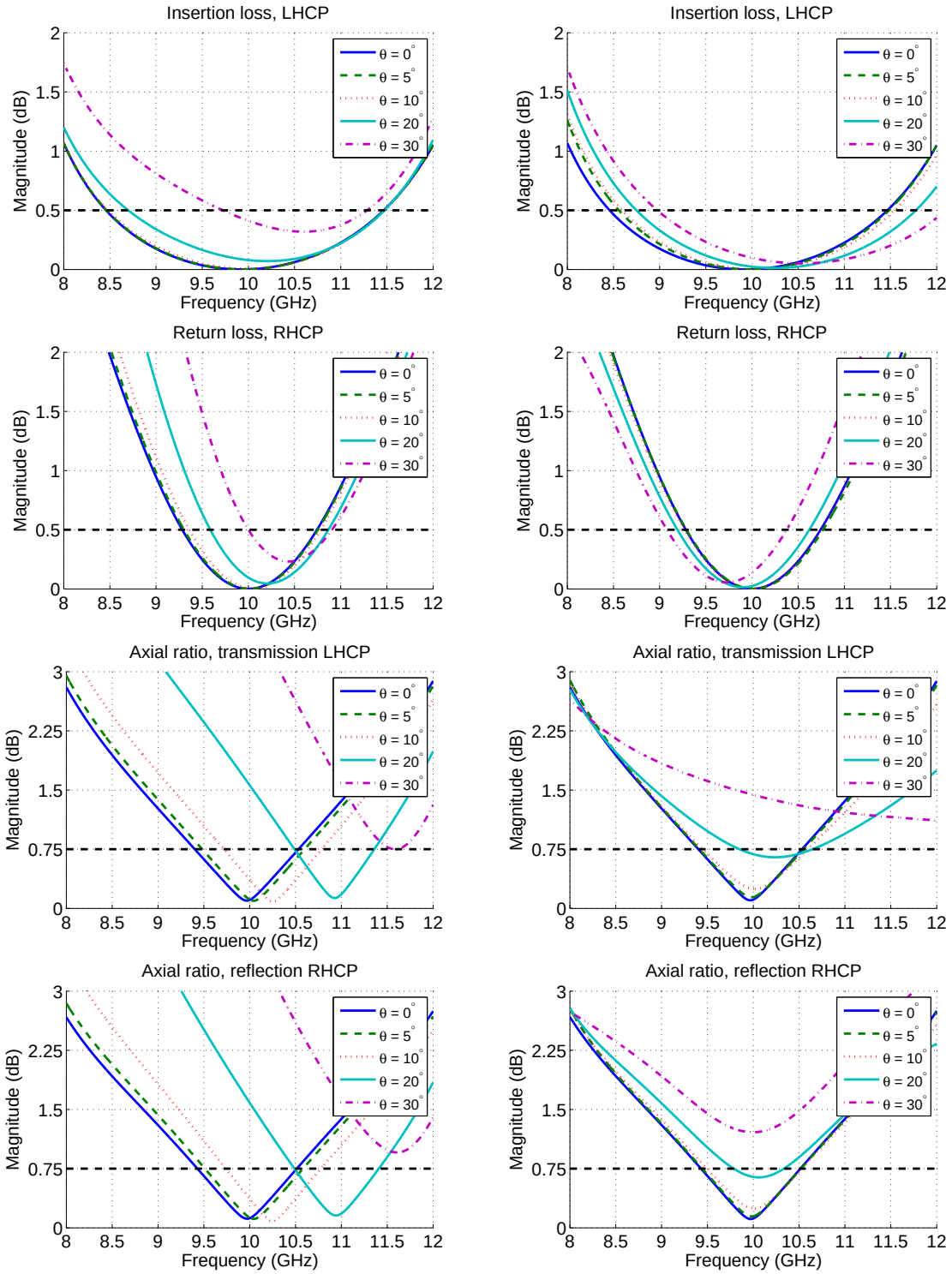

Figure 45: IL, RL and AR for an RHCPSS Helical Tilston structure at various angles of incidence. Left:$\varphi = 0°$, Right: $\varphi = 90°$.

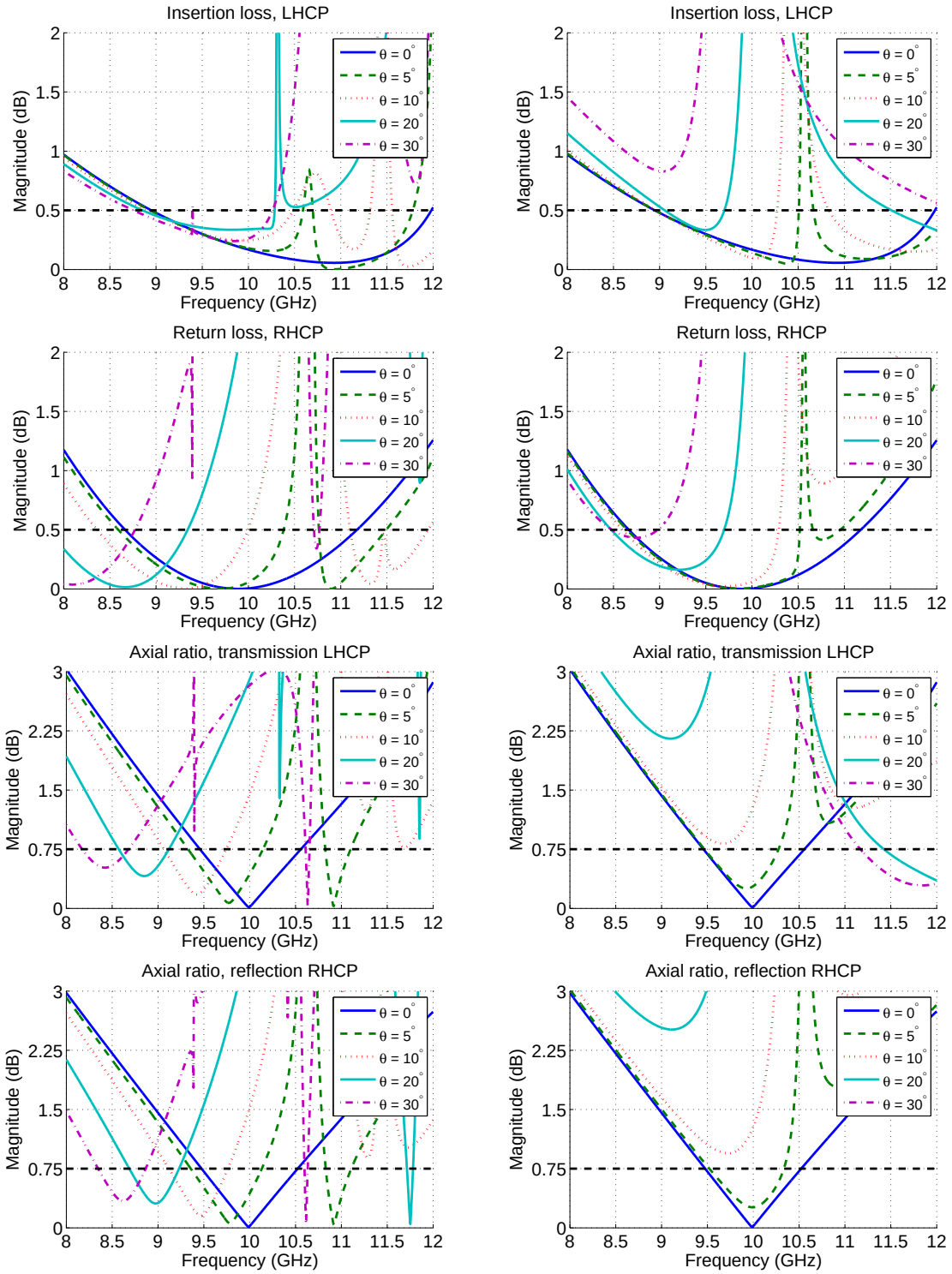

Figure 46: IL, RL and AR for an RHCPSS Single Morin structure at various angles of incidence. Left:$\varphi = 0°$, Right: $\varphi = 90°$.

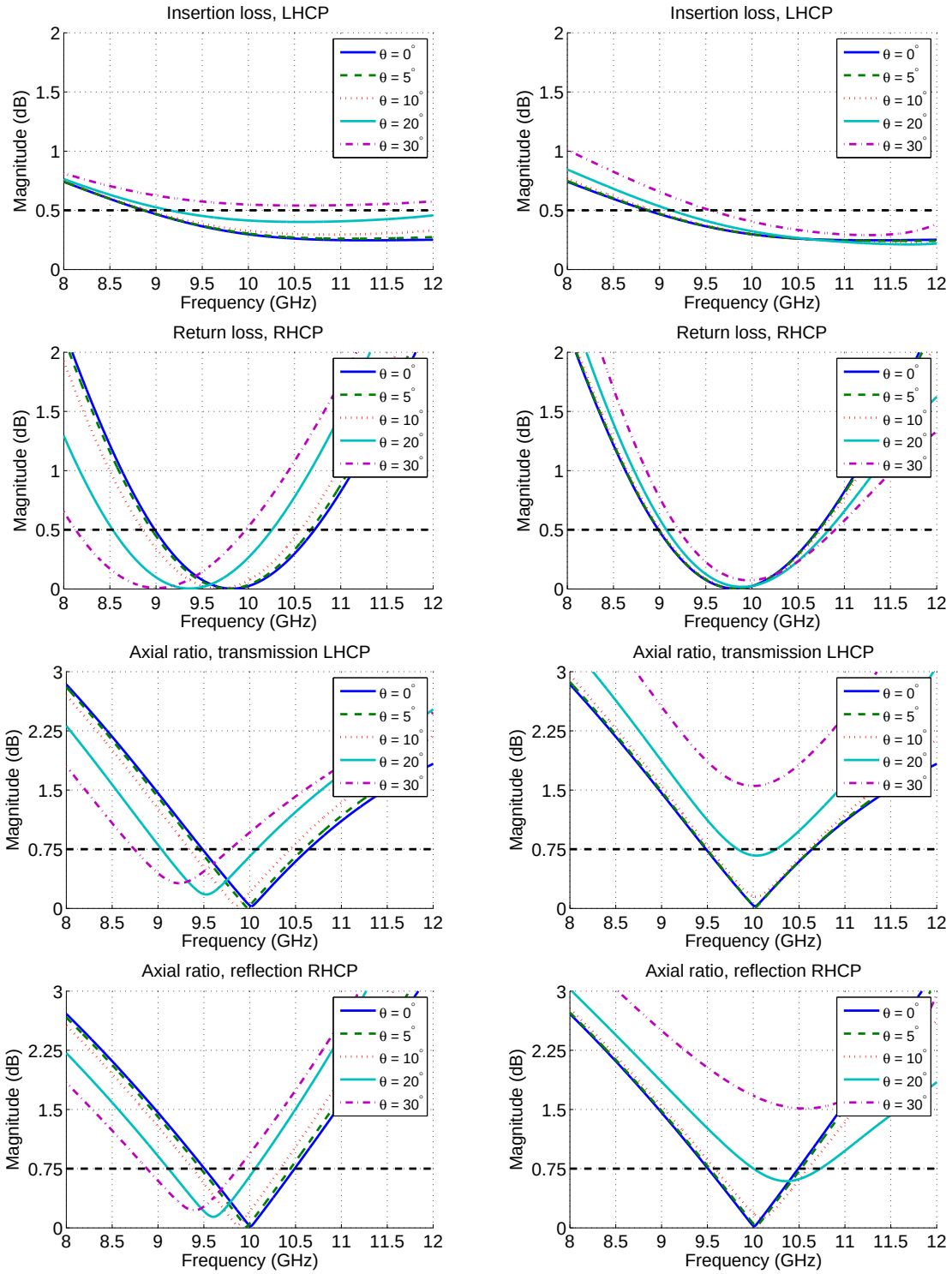

Figure 47: IL, RL and AR for an RHCPSS Double Morin structure at various angles of incidence. Left:$\varphi = 0°$, Right: $\varphi = 90°$.

5.3.6 Morin-Tilston

The results can be seen in Figure 48. As the Morin-Tilston design did not meet the requirements for normal incidence, it does not do so for oblique either. However, the $\varphi = +45°$ plane is quite stable for larger incidence angles so if a modified Morin-Tilston could achieve better performance for normal incidence, it could then possibly perform quite well oblique incidence in that plane.

5.3.7 Crossed Morin

The results can be seen in Figure 49. For both planes the performance impact is largely negligible for up to 10°. At 20° the RL in the $\varphi = -45°$ plane has started to drift slightly, and the AR bandwidth has been noticeable reduced.

For the $\varphi = +45°$ plane however, the performance seems to increase with the incidence angle. It is the only design which can work at 30° and due to this behaviour it would be possible to have a $20° - 30°$ range making it the most versatile of the designs.

5.3.8 Small angles

While the designs are only symmetrical for oblique angles in the specified incidence planes, for small variations in either θ or φ the result is generally close enough that the differences can be disregarded. How large the angles can get depends on the design, however generally somewhere in the range of $5° - 10°$ is acceptable.

If the θ angle is small, then large variations in φ outside of the intended incidence plane can be accepted. On the other hand, even for larger θ angles, small variations on φ is also acceptable. The results of these types of small angle differences for the Crossed Morin design can be seen in Figure 50. Only the AR is displayed as the IL and RL is less affected and as such no difference can be noticed for these small angles.

Note that while the performance is not symmetrical, since the difference is so small they can still be used in these circumstances with slightly reduced performance.

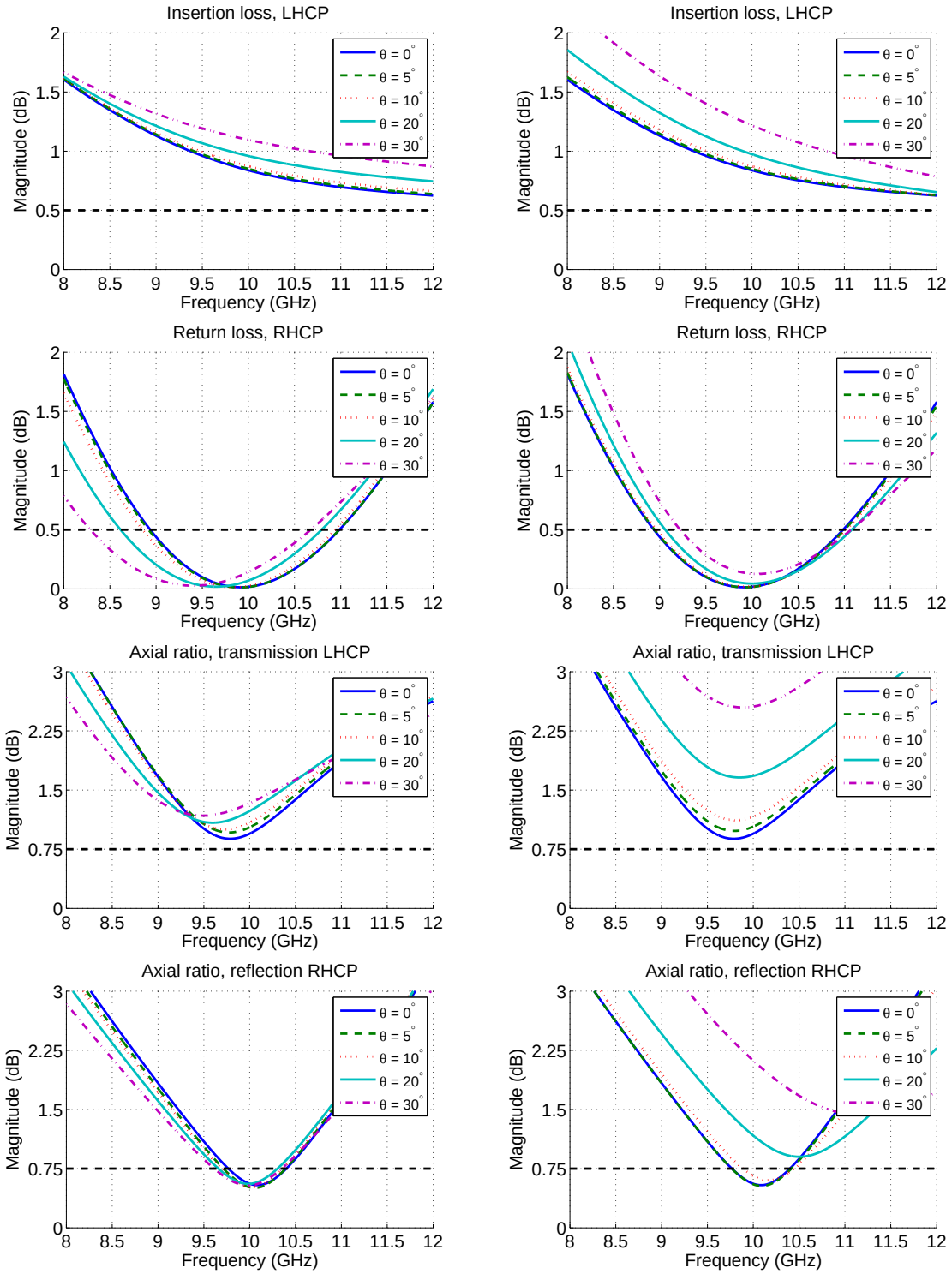

Figure 48: IL, RL and AR for an RHCPSS Morin-Tilston structure at various angles of incidence. Left:$\varphi = +45°$, Right: $\varphi = -45°$.

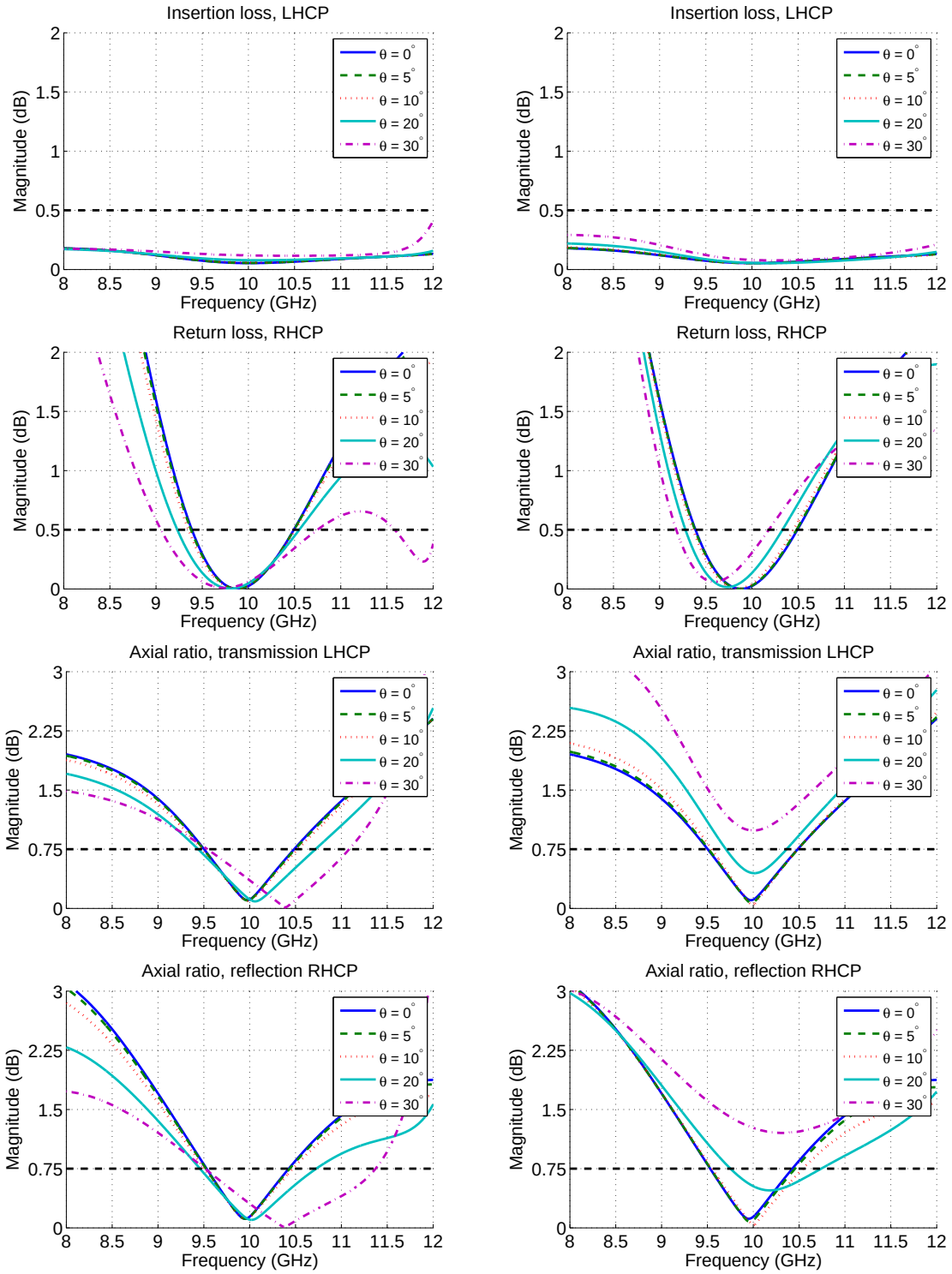

Figure 49: IL, RL and AR for an RHCPSS Crossed Morin structure at various angles of incidence. Left:$\varphi = +45°$, Right: $\varphi = -45°$.

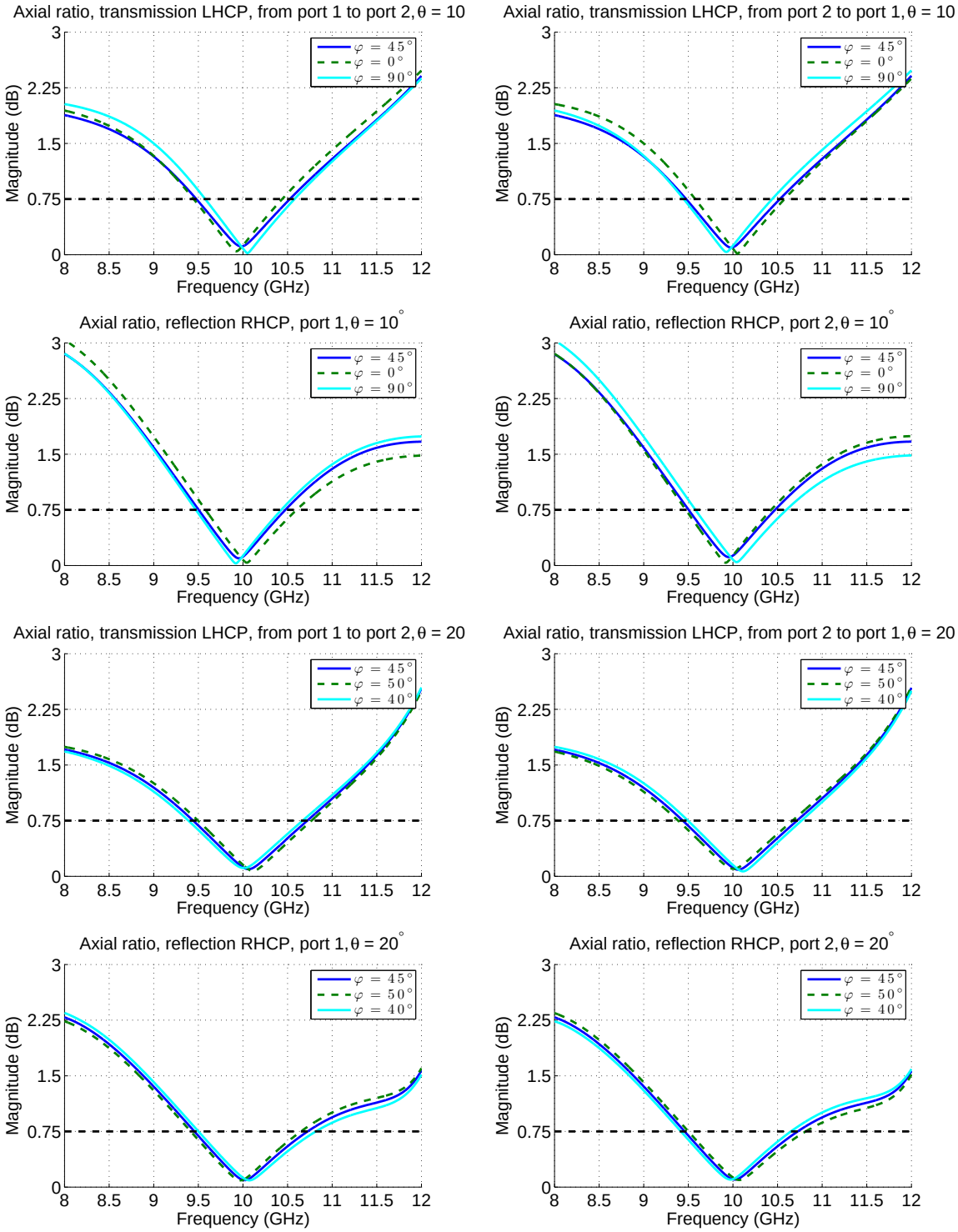

Figure 50: AR for the Crossed Morin structure at various incidence planes for $\theta = 10°$ at the top and $\theta = 20°$ at the bottom.

5.4 Angle Compensation

Most of the structures worked well for smaller angles around normal incidence ($-5°$ to $+5°$ for example), however it would be desirable to be able to achieve the same range around a larger incidence angle, for example $15°$ to $25°$.

After a few attempts at compensating the designs for a higher angle of incidence, it appears that as long as the bandwidth has simply shifted away to other frequencies it is possible to compensate the design such that the bandwidth is centered at 10 GHz for a higher angle.

As an example, consider the Double Morin performance from Figure 47. For the $\varphi = 0°$ plane compensation is possible as the AR and RL is simply shifted to another center frequency, while for the $\varphi = 90°$ plane such compensation is not possible.

Compensation is done by designing the structure for a higher frequency, such that the frequency shift caused by the oblique incidence angle shifts it to the desired center frequency, in this case 10 GHz. The sensitivity to oblique angles is not linear, as a shift from $20°$ to $30°$ is more noticeable than a shift from $0°$ to $10°$. Since the compensation only shift the center frequency the compensated structures will be less stable for variation around the center frequency than the ones designed around normal incidence.

As a proof of concept the Double Morin structure was compensated for an incidence angle of $20°$ (in the $\varphi = 0°$ plane). The results can be seen in Figure 51. The structure was compensated manually and was achieved by taking the previously optimized design, simulating it for $\theta = 20°$ and then gradually adjusting each parameter until the structure performed as desired. The compensated design had the following parameters:

$$\begin{aligned}
\mathbf{l_{xy}} &= 7.51\,\text{mm}\ (\approx 0.25\lambda) \\
\mathbf{l_z} &= 7.10\,\text{mm}\ (\approx 0.24\lambda) \\
\mathbf{s_x} &= 1.25\,\text{mm}\ (\approx 0.042\lambda) \\
\mathbf{p_x} &= 10.621\,\text{mm}\ (\sqrt{2} \cdot l_{xy}) \\
\mathbf{p_y} &= 13.121\,\text{mm}\ (\sqrt{2} \cdot l_{xy} + 2 \cdot s_x) \\
\mathbf{a} &= 0.2\,\text{mm}
\end{aligned}$$

As can be seen in Figure 51 the bandwidth is now centered at 10 GHz at $\theta = 20°$. It can also be seen that it performs almost identically to the uncompensated design aside from the shift to another center frequency.

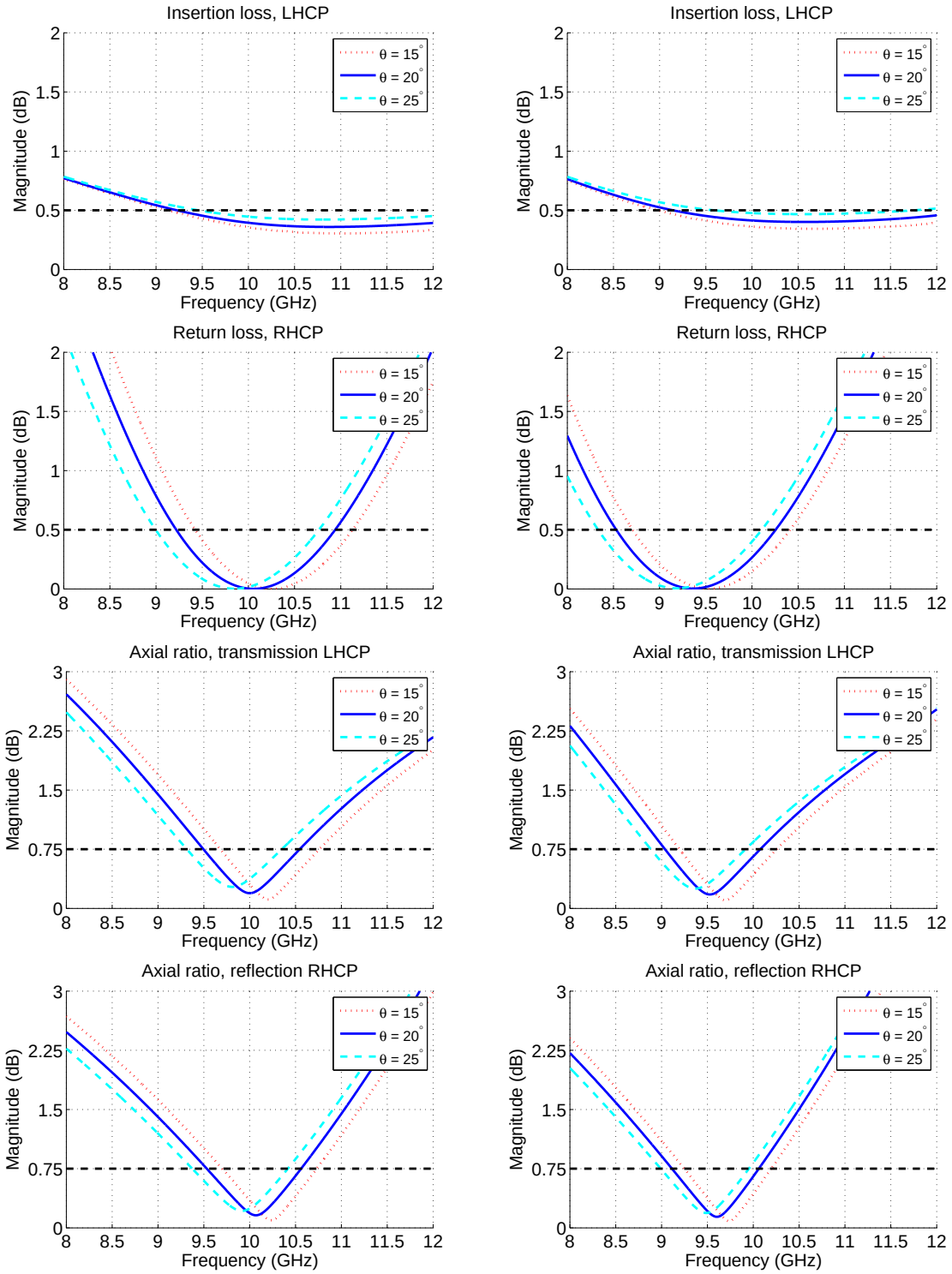

Figure 51: IL, RL and AR for an RHCPSS Double Morin structure compensated for 20° incidence (left) compared with an uncompensated one (right). $\varphi = 0°$.

6 Conclusions

Several different CPSS designs were evaluated for normal and oblique incidence. Most of the designs were limited by the AR bandwidth, which for normal incidence were around $9.5 - 10.5\,\text{GHz}$ giving a percentage bandwidth of about 10%.

Note that aside from the necessary dielectric material needed for the Tilston design to work, no dielectrics were used. Since the Tilston and Pierrot designs require the cell to float freely in air, any actual implementation would require the cell to be embedded in a dielectric slab of some form. This means practical performance for these designs could to some extent, be reduced compared to what is found in this thesis.

For the Morin-Tilston structure no working design was found utilizing only metal wires. However, the design found in [7] achieved performance similar to the Pierrot cell for normal incidence and did this by smart usage of dielectric materials as part of the design. This suggests that adding dielectric materials is not necessarily a negative, as it can be incorporated in the design to achieve a different behaviour.

The Morin based designs can theoretically be attached at the ends and held up without any dielectrics, however it is possible that some dielectrics need to be used to give stability to the structure. How this might affect the performance has not been examined.

During the simulation the metal wires were approximated as Perfect Electrical Conductors. If the wires were to be made using real materials (such as Copper, for example) there would be losses in the wires which are currently not modelled.

It was found that for oblique incidence, the structures are only symmetrical for certain incidence planes and each incidence plane has different performance. This means that it is important to make sure the cells are properly oriented. Since the main usage case outlined was to design a parabolic dish, ensuring all waves hit in the same incidence plane can be difficult. However it was found that it is possible to deviate slightly from the intended incidence plane (around $\pm 5^\circ$ worked well) with minimal impact on the performance.

Most of the designs had at least one incidence plane where they worked well at incidence angles of up to 10°, some worked up to 20° but at that point a smaller bandwidth must usually be accepted as the performance degrades. The Crossed Morin design in the $\varphi = +45^\circ$ plane was an exception as performance seemed stable all the way up to 30°.

It was found that for certain designs the effect of larger oblique angles is a shift

in frequency. This can be compensated for making these structures more viable for use at larger angles. The compensated designs are however more sensitive to deviations in incidence angle than they were for normal incidence, so even a small 5° deviation can have a noticeable impact on the performance.

Overall, the structures are very bandwidth limited with seemingly few ways to improve it. They are quite sensitive to oblique angles and must be oriented properly in order to perform well. The Pierrot and Tilston designs require the cell to be enclosed in a dielectric material which suggests that the Morin based structures are more practical.

All of the designs are quite light and thin, so if the bandwidth performance is acceptable for the application they could be useful, especially the Crossed Morin structure which seems to perform very well for oblique angles. However work must be done to ensure that the cells are properly oriented to get the desired incidence plane. And since the effects of dielectric materials were not properly examined in this thesis, work still needs to be done to evaluate to what extent such materials could be used to improve the performance, or alternatively how much they might negatively affect it.

A CST S-matrix verification

When exporting the S-parameters from CST it is important to know how the exported S-matrix is organized, in this case so that it can be transformed into the theoretical S-matrix introduced in Equation (2.19), which can also be seen below:.

$$\begin{pmatrix} S_{11}^{\mathrm{RR}} & S_{11}^{\mathrm{RL}} & S_{12}^{\mathrm{RR}} & S_{12}^{\mathrm{RL}} \\ S_{11}^{\mathrm{LR}} & S_{11}^{\mathrm{LL}} & S_{12}^{\mathrm{LR}} & S_{12}^{\mathrm{LL}} \\ S_{21}^{\mathrm{RR}} & S_{21}^{\mathrm{RL}} & S_{22}^{\mathrm{RR}} & S_{22}^{\mathrm{RL}} \\ S_{21}^{\mathrm{LR}} & S_{21}^{\mathrm{LL}} & S_{22}^{\mathrm{LR}} & S_{22}^{\mathrm{LL}} \end{pmatrix} \tag{A.1}$$

From studying output and settings in CST it becomes clear that there are two ports, called Zmin (or 1) and Zmax (or 2). These ports can be excited by different modes, by default they are as follows for circular polarization:

$$1 = \mathrm{LHCP}, \qquad 2 = \mathrm{RHCP}$$

This ordering can however be manually changed for each port. Another thing that has been found by studying CST's output is that it refers to each mode as LHCP or RHCP regardless of which direction the wave is travelling in. In other words, CST is in fact using the $\hat{\boldsymbol{e}}_-$ and $\hat{\boldsymbol{e}}_+$ bases internally even if they are called LHCP and RHCP.

The theoretical S-matrix used here defines LHCP and RHCP depending on the propagation direction, as such CST's definition only matches up for waves excited at port 1. This means that if CST claims that port 2 is excited by RHCP, it is by our definition excited by LHCP.

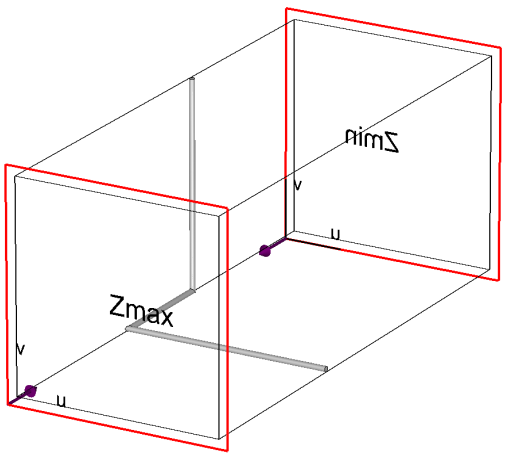

Figure 52: A simple Pierrot cell with both of CST's ports marked.

$$\begin{pmatrix} -0.0984 - 0.1089\text{j} & 0 & 0 & 0 \\ -0.1552 - 0.2295\text{j} & 0 & 0 & 0 \\ 0.4675 + 0.8121\text{j} & 0 & 0 & 0 \\ -0.1510 + 0.0237\text{j} & 0 & 0 & 0 \end{pmatrix}$$
Zmin, LHCP

$$\begin{pmatrix} 0 & 0.8312 - 0.3641\text{j} & 0 & 0 \\ 0 & -0.0984 - 0.1087\text{j} & 0 & 0 \\ 0 & 0.1517 - 0.0181\text{j} & 0 & 0 \\ 0 & 0.3397 - 0.1265\text{j} & 0 & 0 \end{pmatrix}$$
Zmin, RHCP

$$\begin{pmatrix} 0 & 0 & 0 & 0.1517 - 0.0182\text{j} \\ 0 & 0 & 0 & 0.4675 + 0.8121\text{j} \\ 0 & 0 & 0 & 0.1553 + 0.2312\text{j} \\ 0 & 0 & 0 & -0.0930 - 0.1096\text{j} \end{pmatrix}$$
Zmax, LHCP

$$\begin{pmatrix} 0 & 0 & 0.3397 - 0.1264\text{j} & 0 \\ 0 & 0 & -0.1509 + 0.0238\text{j} & 0 \\ 0 & 0 & -0.0929 - 0.1094\text{j} & 0 \\ 0 & 0 & -0.8311 + 0.3655\text{j} & 0 \end{pmatrix}$$
Zmax, RHCP

Table 1: The output from CST. LHCP and RHCP are here defined as in the theoretical S-matrix.

To begin figuring out CST's ordering a simple Pierrot cell was examined (Figure 52). The structure was illuminated at normal incidence by circularly polarized waves. It is possible in CST to specify which modes should be excited in which port. By only exciting, for example, LHCP at port 1 the only S-parameters which can be measured are $S_{11}^{\mathrm{LL}}, S_{11}^{\mathrm{RL}}, S_{21}^{\mathrm{LL}}$ and S_{21}^{RL}. The result of doing this for each port/mode combination and reading the output from CST can be seen in Table 1.

From these matrices, it is possible to deduce half of the necessary information about the exported S-matrix:

$$\begin{pmatrix} S_{\_1}^{\_\mathrm{L}} & S_{\_1}^{\_\mathrm{R}} & S_{\_2}^{\_\mathrm{R}} & S_{\_2}^{\_\mathrm{L}} \\ S_{\_1}^{\_\mathrm{L}} & S_{\_1}^{\_\mathrm{R}} & S_{\_2}^{\_\mathrm{R}} & S_{\_2}^{\_\mathrm{L}} \\ S_{\_1}^{\_\mathrm{L}} & S_{\_1}^{\_\mathrm{R}} & S_{\_2}^{\_\mathrm{R}} & S_{\_2}^{\_\mathrm{L}} \\ S_{\_1}^{\_\mathrm{L}} & S_{\_1}^{\_\mathrm{R}} & S_{\_2}^{\_\mathrm{R}} & S_{\_2}^{\_\mathrm{L}} \end{pmatrix}$$

To get more information about the output the port modes are switched around. The port that is excited stays the same, but for the other port mode 1 becomes RHCP and mode 2 LHCP. This means that the output for this port should change, that is if port 1 is excited by LHCP, S_{21}^{RL} and S_{21}^{LL} should switch places. By redoing the measurements and comparing with the previous ones it is therefore possible to learn more about the output. The output from CST can be seen in Table 2.

Using the information from Table 2 and comparing it to Table 1 it is possible to learn more about the exported matrix:

$$\begin{pmatrix} S_{11}^{\_\mathrm{L}} & S_{11}^{\_\mathrm{R}} & S_{12}^{\_\mathrm{R}} & S_{12}^{\_\mathrm{L}} \\ S_{11}^{\_\mathrm{L}} & S_{11}^{\_\mathrm{R}} & S_{12}^{\_\mathrm{R}} & S_{12}^{\_\mathrm{L}} \\ S_{21}^{\_\mathrm{L}} & S_{21}^{\_\mathrm{R}} & S_{22}^{\_\mathrm{R}} & S_{22}^{\_\mathrm{L}} \\ S_{21}^{\_\mathrm{L}} & S_{21}^{\_\mathrm{R}} & S_{22}^{\_\mathrm{R}} & S_{22}^{\_\mathrm{L}} \end{pmatrix}$$

$$\begin{pmatrix} -0.0984 - 0.1089\text{j} & 0 & 0 & 0 \\ -0.1552 - 0.2295\text{j} & 0 & 0 & 0 \\ -0.1510 + 0.0237\text{j} & 0 & 0 & 0 \\ 0.4675 + 0.8121\text{j} & 0 & 0 & 0 \end{pmatrix} \quad \begin{pmatrix} 0 & 0.8312 - 0.3641\text{j} & 0 & 0 \\ 0 & -0.0984 - 0.1087\text{j} & 0 & 0 \\ 0 & 0.3397 - 0.1265\text{j} & 0 & 0 \\ 0 & 0.1517 - 0.0181\text{j} & 0 & 0 \end{pmatrix}$$

Zmin, LHCP Zmin, RHCP

$$\begin{pmatrix} 0 & 0 & 0 & 0.4675 + 0.8121\text{j} \\ 0 & 0 & 0 & 0.1517 - 0.0182\text{j} \\ 0 & 0 & 0 & 0.1553 + 0.2312\text{j} \\ 0 & 0 & 0 & -0.0930 - 0.1096\text{j} \end{pmatrix} \quad \begin{pmatrix} 0 & 0 & -0.1509 + 0.0238\text{j} & 0 \\ 0 & 0 & 0.3397 - 0.1264\text{j} & 0 \\ 0 & 0 & -0.0929 - 0.1094\text{j} & 0 \\ 0 & 0 & -0.8311 + 0.3655\text{j} & 0 \end{pmatrix}$$

Zmax, LHCP Zmax, RHCP

Table 2: The output from CST after switching the modes. LHCP and RHCP are here defined as in the theoretical S-matrix.

It is now known which S-parameters are reflection and which are transmission. The Pierrot element for normal incidence is symmetric which means that, for example, $S_{12}^{\mathrm{LL}} = S_{21}^{\mathrm{LL}}$, by using this and checking which S-parameters are identical it is possible to get more information about the S-matrix:

$$\begin{pmatrix} S_{11}^{\_\mathrm{L}} & S_{11}^{\_\mathrm{R}} & S_{12}^{\mathrm{RR}} & S_{12}^{\mathrm{RL}} \\ S_{11}^{\_\mathrm{L}} & S_{11}^{\_\mathrm{R}} & S_{12}^{\mathrm{LR}} & S_{12}^{\mathrm{LL}} \\ S_{21}^{\mathrm{LL}} & S_{21}^{\mathrm{LR}} & S_{22}^{\_\mathrm{R}} & S_{22}^{\_\mathrm{L}} \\ S_{21}^{\mathrm{RL}} & S_{21}^{\mathrm{RR}} & S_{22}^{\_\mathrm{R}} & S_{22}^{\_\mathrm{L}} \end{pmatrix}$$

Assuming symmetry in the placement (an assumption that will later be verified) the final S-matrix should look like this:

$$\begin{pmatrix} S_{11}^{\mathrm{RL}} & S_{11}^{\mathrm{RR}} & S_{12}^{\mathrm{RR}} & S_{12}^{\mathrm{RL}} \\ S_{11}^{\mathrm{LL}} & S_{11}^{\mathrm{LR}} & S_{12}^{\mathrm{LR}} & S_{12}^{\mathrm{LL}} \\ S_{21}^{\mathrm{LL}} & S_{21}^{\mathrm{LR}} & S_{22}^{\mathrm{LR}} & S_{22}^{\mathrm{LL}} \\ S_{21}^{\mathrm{RL}} & S_{21}^{\mathrm{RR}} & S_{22}^{\mathrm{RR}} & S_{22}^{\mathrm{RL}} \end{pmatrix}$$

This means that to get the theoretical matrix the following transformation is needed:

$$\boldsymbol{S} = \begin{pmatrix} 1 & 0 & 0 & 0 \\ 0 & 1 & 0 & 0 \\ 0 & 0 & 0 & 1 \\ 0 & 0 & 1 & 0 \end{pmatrix} \begin{pmatrix} S_{11}^{\mathrm{CST}} & S_{11}^{\mathrm{CST}} & S_{12}^{\mathrm{CST}} & S_{12}^{\mathrm{CST}} \\ S_{11}^{\mathrm{CST}} & S_{11}^{\mathrm{CST}} & S_{12}^{\mathrm{CST}} & S_{12}^{\mathrm{CST}} \\ S_{21}^{\mathrm{CST}} & S_{21}^{\mathrm{CST}} & S_{22}^{\mathrm{CST}} & S_{22}^{\mathrm{CST}} \\ S_{21}^{\mathrm{CST}} & S_{21}^{\mathrm{CST}} & S_{22}^{\mathrm{CST}} & S_{22}^{\mathrm{CST}} \end{pmatrix} \begin{pmatrix} 0 & 1 & 0 & 0 \\ 1 & 0 & 0 & 0 \\ 0 & 0 & 1 & 0 \\ 0 & 0 & 0 & 1 \end{pmatrix} \tag{A.2}$$

To verify this assumption a known structure is simulated. It is possible to create a linear polarizer using a simple grating as can be seen in Figure 53, consisting of thin metal wires running in one direction. If the grating is placed between the

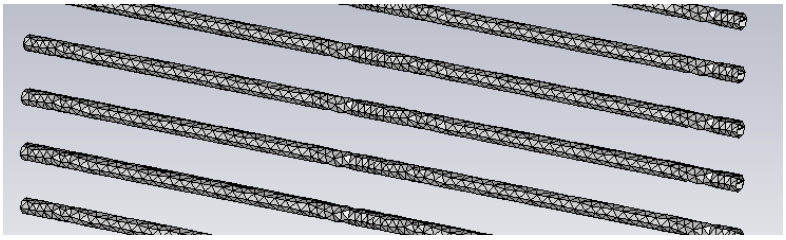

Figure 53: A linear polarizer consisting of PEC wires.

two ports and running in the x-direction the S-matrix in linear polarization should theoretically be:

$$\boldsymbol{S}^{\mathrm{LP}}_{\mathrm{theory}} = \begin{pmatrix} S^{\mathrm{XX}}_{11} & S^{\mathrm{XY}}_{11} & S^{\mathrm{XX}}_{12} & S^{\mathrm{XY}}_{12} \\ S^{\mathrm{YX}}_{11} & S^{\mathrm{YY}}_{11} & S^{\mathrm{YX}}_{12} & S^{\mathrm{YY}}_{12} \\ S^{\mathrm{XX}}_{21} & S^{\mathrm{XY}}_{21} & S^{\mathrm{XX}}_{22} & S^{\mathrm{XY}}_{22} \\ S^{\mathrm{YX}}_{21} & S^{\mathrm{YY}}_{21} & S^{\mathrm{YX}}_{22} & S^{\mathrm{YY}}_{22} \end{pmatrix} = \mathrm{e}^{-\mathrm{j}\phi} \begin{pmatrix} -1 & 0 & 0 & 0 \\ 0 & 0 & 0 & 1 \\ 0 & 0 & -1 & 0 \\ 0 & 1 & 0 & 0 \end{pmatrix} \tag{A.3}$$

The total fields in ports 1 and 2 can be written as:

$$\boldsymbol{E}^{(\mathrm{out})}_1 = E^{\mathrm{X}}_1 \hat{\boldsymbol{x}} + E^{\mathrm{Y}}_1 \hat{\boldsymbol{y}} = E^{\mathrm{R}}_1 \hat{\boldsymbol{e}}_- + E^{\mathrm{L}}_1 \hat{\boldsymbol{e}}_+ \quad \boldsymbol{E}^{(\mathrm{in})}_1 = E^{\mathrm{X}}_{10} \hat{\boldsymbol{x}} + E^{\mathrm{Y}}_{10} \hat{\boldsymbol{y}} = E^{\mathrm{R}}_{10} \hat{\boldsymbol{e}}_+ + E^{\mathrm{L}}_{10} \hat{\boldsymbol{e}}_-$$
$$\boldsymbol{E}^{(\mathrm{out})}_2 = E^{\mathrm{X}}_2 \hat{\boldsymbol{x}} + E^{\mathrm{Y}}_2 \hat{\boldsymbol{y}} = E^{\mathrm{R}}_2 \hat{\boldsymbol{e}}_+ + E^{\mathrm{L}}_2 \hat{\boldsymbol{e}}_- \quad \boldsymbol{E}^{(\mathrm{in})}_2 = E^{\mathrm{X}}_{20} \hat{\boldsymbol{x}} + E^{\mathrm{Y}}_{20} \hat{\boldsymbol{y}} = E^{\mathrm{R}}_{20} \hat{\boldsymbol{e}}_- + E^{\mathrm{L}}_{20} \hat{\boldsymbol{e}}_+$$

Based on the unit vector relations introduced in Equation (2.8), this implies a relation between circular and linear fields as follows:

$$\begin{pmatrix} E^{\mathrm{R}}_1 \\ E^{\mathrm{L}}_1 \\ E^{\mathrm{R}}_2 \\ E^{\mathrm{L}}_2 \end{pmatrix} = \frac{1}{\sqrt{2}} \begin{pmatrix} 1 & -\mathrm{j} & 0 & 0 \\ 1 & \mathrm{j} & 0 & 0 \\ 0 & 0 & 1 & \mathrm{j} \\ 0 & 0 & 1 & -\mathrm{j} \end{pmatrix} \begin{pmatrix} E^{\mathrm{X}}_1 \\ E^{\mathrm{Y}}_1 \\ E^{\mathrm{X}}_2 \\ E^{\mathrm{Y}}_2 \end{pmatrix}, \begin{pmatrix} E^{\mathrm{X}}_{10} \\ E^{\mathrm{Y}}_{10} \\ E^{\mathrm{X}}_{20} \\ E^{\mathrm{Y}}_{20} \end{pmatrix} = \frac{1}{\sqrt{2}} \begin{pmatrix} 1 & 1 & 0 & 0 \\ \mathrm{j} & -\mathrm{j} & 0 & 0 \\ 0 & 0 & 1 & 1 \\ 0 & 0 & \mathrm{j} & -\mathrm{j} \end{pmatrix} \begin{pmatrix} E^{\mathrm{R}}_{10} \\ E^{\mathrm{L}}_{10} \\ E^{\mathrm{R}}_{20} \\ E^{\mathrm{L}}_{20} \end{pmatrix}$$

This gives the transformation between circular and linear S-matrices as:

$$\begin{aligned} S^{\mathrm{CP}} &= \begin{pmatrix} S^{\mathrm{RR}}_{11} & S^{\mathrm{RL}}_{11} & S^{\mathrm{RR}}_{12} & S^{\mathrm{RL}}_{12} \\ S^{\mathrm{LR}}_{11} & S^{\mathrm{LL}}_{11} & S^{\mathrm{LR}}_{12} & S^{\mathrm{LL}}_{12} \\ S^{\mathrm{RR}}_{21} & S^{\mathrm{RL}}_{21} & S^{\mathrm{RR}}_{22} & S^{\mathrm{RL}}_{22} \\ S^{\mathrm{LR}}_{21} & S^{\mathrm{LL}}_{21} & S^{\mathrm{LR}}_{22} & S^{\mathrm{LL}}_{22} \end{pmatrix} \\ &= \frac{1}{2} \begin{pmatrix} 1 & -\mathrm{j} & 0 & 0 \\ 1 & \mathrm{j} & 0 & 0 \\ 0 & 0 & 1 & \mathrm{j} \\ 0 & 0 & 1 & -\mathrm{j} \end{pmatrix} \begin{pmatrix} S^{\mathrm{XX}}_{11} & S^{\mathrm{XY}}_{11} & S^{\mathrm{XX}}_{12} & S^{\mathrm{XY}}_{12} \\ S^{\mathrm{YX}}_{11} & S^{\mathrm{YY}}_{11} & S^{\mathrm{YX}}_{12} & S^{\mathrm{YY}}_{12} \\ S^{\mathrm{XX}}_{21} & S^{\mathrm{XY}}_{21} & S^{\mathrm{XX}}_{22} & S^{\mathrm{XY}}_{22} \\ S^{\mathrm{YX}}_{21} & S^{\mathrm{YY}}_{21} & S^{\mathrm{YX}}_{22} & S^{\mathrm{YY}}_{22} \end{pmatrix} \begin{pmatrix} 1 & 1 & 0 & 0 \\ -\mathrm{j} & \mathrm{j} & 0 & 0 \\ 0 & 0 & 1 & 1 \\ 0 & 0 & \mathrm{j} & -\mathrm{j} \end{pmatrix} \end{aligned} \tag{A.4}$$

This transformation then gives the linear polarizer in circular polarization as:

$$\boldsymbol{S}^{\mathrm{CP}}_{\mathrm{theory}} = \mathrm{e}^{-\mathrm{j}\phi}\frac{1}{2}\begin{pmatrix}1 & -\mathrm{j} & 0 & 0\\ 1 & \mathrm{j} & 0 & 0\\ 0 & 0 & 1 & \mathrm{j}\\ 0 & 0 & 1 & -\mathrm{j}\end{pmatrix}\begin{pmatrix}-1 & 0 & 0 & 0\\ 0 & 0 & 0 & 1\\ 0 & 0 & -1 & 0\\ 0 & 1 & 0 & 0\end{pmatrix}\begin{pmatrix}1 & 1 & 0 & 0\\ -\mathrm{j} & \mathrm{j} & 0 & 0\\ 0 & 0 & 1 & 1\\ 0 & 0 & \mathrm{j} & -\mathrm{j}\end{pmatrix}$$
$$= \frac{\mathrm{e}^{-\mathrm{j}\phi}}{2}\begin{pmatrix}-1 & -1 & +1 & -1\\ -1 & -1 & -1 & +1\\ +1 & -1 & -1 & -1\\ -1 & +1 & -1 & -1\end{pmatrix} \quad \text{(A.5)}$$

After simulating the grating in CST, applying the transformation from Equation (A.2) and normalizing with the negative of the top left element, the S-matrix becomes as follows:

$$\begin{pmatrix}-1.0000 & 0.9986+0.0723\mathrm{j} & -0.9985-0.0616\mathrm{j} & -1.0015+0.0218\mathrm{j}\\ 0.9986+0.0723\mathrm{j} & -1.0001-0.0000\mathrm{j} & -1.0015+0.0219\mathrm{j} & -0.9985-0.0617\mathrm{j}\\ -0.9985-0.0617\mathrm{j} & -1.0015+0.0219\mathrm{j} & -1.0000+0.0005\mathrm{j} & 0.9986+0.0718\mathrm{j}\\ -1.0015+0.0219\mathrm{j} & -0.9985-0.0617\mathrm{j} & 0.9986+0.0718\mathrm{j} & -1.0000+0.0005\mathrm{j}\end{pmatrix}$$

which is clearly not the expected theoretical results. After re-examining the results it appears that CST adds a minus sign in front of some S-parameters. Changing the transformation to:

$$\boldsymbol{S} = \begin{pmatrix}1 & 0 & 0 & 0\\ 0 & 1 & 0 & 0\\ 0 & 0 & 0 & 1\\ 0 & 0 & 1 & 0\end{pmatrix}\begin{pmatrix}S^{\mathrm{CST}}_{11} & -S^{\mathrm{CST}}_{11} & S^{\mathrm{CST}}_{12} & -S^{\mathrm{CST}}_{12}\\ -S^{\mathrm{CST}}_{11} & S^{\mathrm{CST}}_{11} & -S^{\mathrm{CST}}_{12} & S^{\mathrm{CST}}_{12}\\ S^{\mathrm{CST}}_{21} & -S^{\mathrm{CST}}_{21} & S^{\mathrm{CST}}_{22} & -S^{\mathrm{CST}}_{22}\\ -S^{\mathrm{CST}}_{21} & S^{\mathrm{CST}}_{21} & -S^{\mathrm{CST}}_{22} & S^{\mathrm{CST}}_{22}\end{pmatrix}\begin{pmatrix}0 & 1 & 0 & 0\\ 1 & 0 & 0 & 0\\ 0 & 0 & 1 & 0\\ 0 & 0 & 0 & 1\end{pmatrix} \quad \text{(A.6)}$$

With this transformation the results for the linear polarizer becomes:

$$\begin{pmatrix}-1.0000 & -0.9986-0.0723\mathrm{j} & 0.9985+0.0616\mathrm{j} & -1.0015+0.0218\mathrm{j}\\ -0.9986-0.0723\mathrm{j} & -1.0001-0.0000\mathrm{j} & -1.0015+0.0219\mathrm{j} & 0.9985+0.0617\mathrm{j}\\ 0.9985+0.0617\mathrm{j} & -1.0015+0.0219\mathrm{j} & -1.0000+0.0005\mathrm{j} & -0.9986-0.0718\mathrm{j}\\ -1.0015+0.0219\mathrm{j} & 0.9985+0.0617\mathrm{j} & -0.9986-0.0718\mathrm{j} & -1.0000+0.0005\mathrm{j}\end{pmatrix}$$

Which is in line with the theoretically expected result, aside from slight differences due to the numerical accuracy of the simulation.

To further verify the transformation it is verified compared to published results. In [14] a Pierrot cell was experimentally tested together with detailed dimensions which allows it to be accurately recreated in CST. The geometry can be seen in Figure 54. The results in Figure 55 agree with results published in [14].

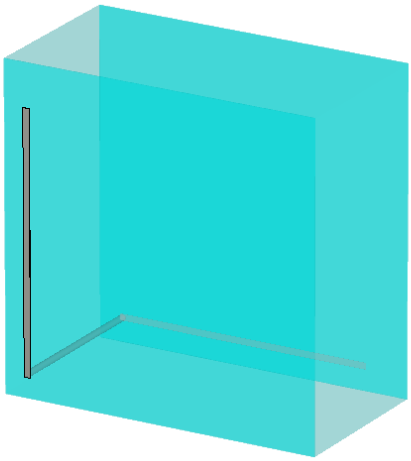

Figure 54: The Pierrot cell from [14]. The cell is encased in a dielectric material to hold it in place.

As a final verification, oblique incidence must also be verified. Based on the unit vectors from Equation (2.8), relations between linear and circular vectors can be found as:

$$\hat{\boldsymbol{e}}_+ = \frac{\hat{\boldsymbol{x}}\cos(\theta) - \mathrm{j}\hat{\boldsymbol{y}}}{\sqrt{2}} \qquad \hat{\boldsymbol{e}}_- = \frac{\hat{\boldsymbol{x}}\cos(\theta) + \mathrm{j}\hat{\boldsymbol{y}}}{\sqrt{2}} \tag{A.7}$$

$$\hat{\boldsymbol{x}} = \frac{\hat{\boldsymbol{e}}_+ + \hat{\boldsymbol{e}}_-}{\sqrt{2}\cos(\theta)} \qquad \hat{\boldsymbol{y}} = \mathrm{j}\frac{\hat{\boldsymbol{e}}_+ - \hat{\boldsymbol{e}}_-}{\sqrt{2}} \tag{A.8}$$

at which point the wave traces an ellipse instead of a circle. This gives the following relations between circular and linear fields:

$$\begin{pmatrix} E_1^{\mathrm{R}} \\ E_1^{\mathrm{L}} \\ E_2^{\mathrm{R}} \\ E_2^{\mathrm{L}} \end{pmatrix} = \frac{1}{\sqrt{2}} \begin{pmatrix} 1/\cos\theta & -\mathrm{j} & 0 & 0 \\ 1/\cos\theta & \mathrm{j} & 0 & 0 \\ 0 & 0 & 1/\cos\theta & \mathrm{j} \\ 0 & 0 & 1/\cos\theta & -\mathrm{j} \end{pmatrix} \begin{pmatrix} E_1^{\mathrm{X}} \\ E_1^{\mathrm{Y}} \\ E_2^{\mathrm{X}} \\ E_2^{\mathrm{Y}} \end{pmatrix}$$

$$\begin{pmatrix} E_{10}^{\mathrm{X}} \\ E_{10}^{\mathrm{Y}} \\ E_{20}^{\mathrm{X}} \\ E_{20}^{\mathrm{Y}} \end{pmatrix} = \frac{1}{\sqrt{2}} \begin{pmatrix} \cos\theta & \cos\theta & 0 & 0 \\ -\mathrm{j} & \mathrm{j} & 0 & 0 \\ 0 & 0 & \cos\theta & \cos\theta \\ 0 & 0 & \mathrm{j} & -\mathrm{j} \end{pmatrix} \begin{pmatrix} E_{10}^{\mathrm{R}} \\ E_{10}^{\mathrm{L}} \\ E_{20}^{\mathrm{R}} \\ E_{20}^{\mathrm{L}} \end{pmatrix}$$

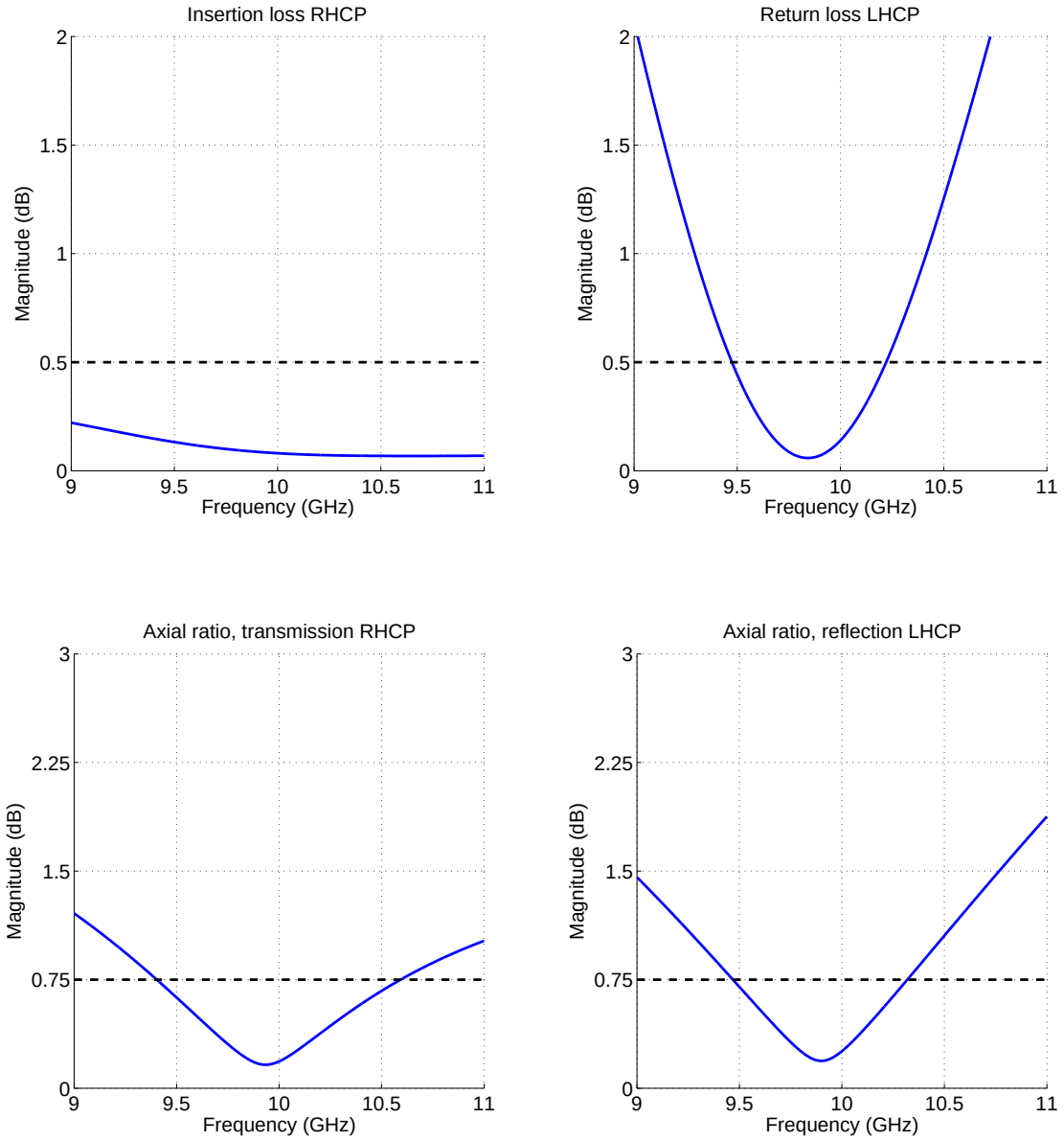

Figure 55: IL, RL and AR for the LHCPSS Pierrot from [14]

which gives a transformation of:

$$\boldsymbol{S}^{\mathrm{CP}} = \frac{1}{2}\begin{pmatrix} 1/\cos\theta & -\mathrm{j} & 0 & 0 \\ 1/\cos\theta & \mathrm{j} & 0 & 0 \\ 0 & 0 & 1/\cos\theta & \mathrm{j} \\ 0 & 0 & 1/\cos\theta & -\mathrm{j} \end{pmatrix} \begin{pmatrix} S_{11}^{\mathrm{XX}} & S_{11}^{\mathrm{XY}} & S_{12}^{\mathrm{XX}} & S_{12}^{\mathrm{XY}} \\ S_{11}^{\mathrm{YX}} & S_{11}^{\mathrm{YY}} & S_{12}^{\mathrm{YX}} & S_{12}^{\mathrm{YY}} \\ S_{21}^{\mathrm{XX}} & S_{21}^{\mathrm{XY}} & S_{22}^{\mathrm{XX}} & S_{22}^{\mathrm{XY}} \\ S_{21}^{\mathrm{YX}} & S_{21}^{\mathrm{YY}} & S_{22}^{\mathrm{YX}} & S_{22}^{\mathrm{YY}} \end{pmatrix} \begin{pmatrix} \cos\theta & \cos\theta & 0 & 0 \\ -\mathrm{j} & \mathrm{j} & 0 & 0 \\ 0 & 0 & \cos\theta & \cos\theta \\ 0 & 0 & \mathrm{j} & -\mathrm{j} \end{pmatrix} \tag{A.9}$$

ultimately resulting in the transformation of the linear polarizer as:

$$\begin{aligned} \boldsymbol{S}_{\mathrm{theory}}^{\mathrm{CP}} = \mathrm{e}^{-\mathrm{j}\phi}\frac{1}{2}\begin{pmatrix} 1/\cos\theta & -\mathrm{j} & 0 & 0 \\ 1/\cos\theta & \mathrm{j} & 0 & 0 \\ 0 & 0 & 1/\cos\theta & \mathrm{j} \\ 0 & 0 & 1/\cos\theta & -\mathrm{j} \end{pmatrix} \begin{pmatrix} -1 & 0 & 0 & 0 \\ 0 & 0 & 0 & 1 \\ 0 & 0 & -1 & 0 \\ 0 & 1 & 0 & 0 \end{pmatrix} \begin{pmatrix} \cos\theta & \cos\theta & 0 & 0 \\ -\mathrm{j} & \mathrm{j} & 0 & 0 \\ 0 & 0 & \cos\theta & \cos\theta \\ 0 & 0 & \mathrm{j} & -\mathrm{j} \end{pmatrix} \\ = \frac{\mathrm{e}^{-\mathrm{j}\phi}}{2}\begin{pmatrix} -1 & -1 & +1 & -1 \\ -1 & -1 & -1 & +1 \\ +1 & -1 & -1 & -1 \\ -1 & +1 & -1 & -1 \end{pmatrix} \end{aligned} \tag{A.10}$$

The result is identical to the case with normal incidence, which means that for oblique incidence the S-matrix should not change. The result of simulating the polarizer at $\theta = 15°$ is:

$$\begin{pmatrix} -1.0000 & -0.9987 - 0.0698\mathrm{j} & 0.9986 + 0.0597\mathrm{j} & -1.0014 + 0.0211\mathrm{j} \\ -0.9987 - 0.0698\mathrm{j} & -1.0001 - 0.0000\mathrm{j} & -1.0014 + 0.0211\mathrm{j} & 0.9986 + 0.0597\mathrm{j} \\ 0.9986 + 0.0597\mathrm{j} & -1.0014 + 0.0211\mathrm{j} & -1.0000 + 0.0005\mathrm{j} & -0.9987 - 0.0693\mathrm{j} \\ -1.0014 + 0.0211\mathrm{j} & 0.9986 + 0.0597\mathrm{j} & -0.9987 - 0.0693\mathrm{j} & -1.0000 + 0.0005\mathrm{j} \end{pmatrix}$$

and for $\theta = 30°$:

$$\begin{pmatrix} -1.0000 & -0.9989 - 0.0629\mathrm{j} & 0.9989 + 0.0537\mathrm{j} & -1.0011 + 0.0187\mathrm{j} \\ -0.9989 - 0.0629\mathrm{j} & -1.0000 - 0.0000\mathrm{j} & -1.0011 + 0.0187\mathrm{j} & 0.9988 + 0.0537\mathrm{j} \\ 0.9989 + 0.0537\mathrm{j} & -1.0011 + 0.0187\mathrm{j} & -1.0000 + 0.0005\mathrm{j} & -0.9989 - 0.0625\mathrm{j} \\ -1.0011 + 0.0187\mathrm{j} & 0.9988 + 0.0537\mathrm{j} & -0.9989 - 0.0625\mathrm{j} & -1.0000 + 0.0005\mathrm{j} \end{pmatrix}$$

They are both in line with the expected result.

References

[1] *IEEE Standard Dictionary of Electrical and Electronic Terms, Fourth Edition.* IEEE Press, 1988.

[2] IEEE Standard Definitions of Terms for Antennas. *IEEE Std 145-1993*, 1993.

[3] Matteo Albani, Peter Balling, Leri Datashvili, Giampiero Gerini, P Ingvarson, Knut Pontoppidan, Marco Sabbadini, D Sjoberg, S Skokic, and Giuseppe Vecchi. Concepts for polarising sheets & dual-gridded reflectors for circular polarisation. In *ICECom, 2010 Conference Proceedings*, pages 1–4. IEEE, 2010.

[4] S. Cornbleet. *Microwave Optics: The Optics of Microwave Antenna Design.* Pure and applied physics. Academic Press, 1976.

[5] B.R. Elbert. *Introduction to Satellite Communication.* ARTECH HOUSE Incorporated, 2008.

[6] ESA. Appendix 1 to ESTEC ITT AO/1-7242/12/NL/MH, Circular Polarisation Dual-Optics Proof-of-Concept. 2011.

[7] G. Giampiero et al. Circular Polarisation Dual-Optics Proof-of-Concept, Technical Proposal submitted by TU Eindhoven, RUAG Space AB, Lund University, and ASC ApS to ESA in response to ESTEC ITT AO/1-7242/12/NL/MH. Oct 2012.

[8] John D. Jackson. *Classical Electrodynamics Third Edition.* Wiley, third edition, 1998.

[9] M.A. Joyal and J.J. Laurin. A cascaded Circular-Polarization-Selective Surface at K band. In *Antennas and Propagation (APSURSI), 2011 IEEE International Symposium on*, pages 2657–2660. IEEE, 2011.

[10] S.C. Kwon and G.L. Stuber. Geometrical theory of channel depolarization. *Vehicular Technology, IEEE Transactions on*, 60(8):3542–3556, 2011.

[11] G.A. Morin. A circular polarization selective surface made of resonant helices. Technical report, DTIC Document, 1995.

[12] S.J. Orfanidis. *Electromagnetic waves and antennas.* Rutgers University Piscataway, NJ, www.ece.rutgers.edu/õrfanidi/ewa, 2008.

[13] J.E. Roy and L. Shafai. Reciprocal circular-polarization-selective surface. *Antennas and Propagation Magazine, IEEE*, 38(6):18–33, 1996.

[14] J. Sanz-Fernandez, E. Saenz, P. de Maagt, and C. Mangenot. Circular polarization selective surface for dual-optics CP offset reflector antennas in Ku-band. In *Antennas and Propagation (EUCAP), 2012 6th European Conference on*, pages 2683–2687. IEEE, 2012.

[15] J.L. Volakis, A. Chatterjee, and L.C. Kempel. *Finite Element Method for Electromagnetics: Antennas, Microwave Circuits, and Scattering Applications*. IEEE Press Series on Electromagnetic Wave Theory. Wiley, 1998.

[16] T. Weiland. RF microwave simulators - from component to system design. In *Microwave Conference, 2003. 33rd European*, volume 2, pages 591–596 vol.2, Oct. 2003.